

Department for Biomedical Sciences at the University of Veterinary Medicine Vienna

Institute of Laboratory Animal Science  
(Head: Univ.-Prof. Dr. Thomas Rüllicke)

**Biodistribution studies of intratracheally applied nucleic acid-  
based drugs using multimodal optical tomography**

Diploma Thesis

University of Veterinary Medicine Vienna

Submitted by  
Wolfram Emanuel Polzer

Vienna, September 2019

Supervisor: Univ.-Prof. Dr. Thomas Rüllicke; Institute of Laboratory Animal Science,  
University of Veterinary Medicine, Vienna

External Supervisor: Univ.-Prof. Dipl. Ing. Dr. Manfred Ogris; Division of Clinical Pharmacy  
and Diagnostics, University of Vienna

External Co- Supervisor: Dr. Haider Sami; Division of Clinical Pharmacy and Diagnostics,  
University of Vienna

Reviewer: Univ.-Prof. Dr.med. Dr.med.vet. Reinhold Erben; Institute of Physiology,  
Pathophysiology and Biophysics, Unit of Physiology, Pathophysiology and Experimental  
Endocrinology, University of Veterinary Medicine, Vienna

## Table of Contents

1. Introduction .....	5
1.1. <i>In vivo</i> imaging.....	5
1.2. Magnetic resonance imaging (MRI) .....	6
1.3. Computed tomography (CT).....	7
1.4. Optical imaging.....	8
1.4.1. Fluorescence imaging (FLI) .....	10
1.4.1.1. Quantum dots (QDs) as near infrared (NIR) contrast agents.....	13
1.4.2. Bioluminescence Imaging (BLI).....	15
1.4.2.1. Tracking gene delivery efficiency- CD49f targeted polyplexes .....	18
1.4.2.2. Tracking biological processes: tumor growth with CD47 .....	20
1.5. Intratracheal instillation.....	23
2. Aim of the Thesis .....	27
3. Materials and methods .....	28
3.1. Animals.....	28
3.2. Intratracheal instillation.....	33
3.3. Imaging.....	35
4. Results and discussion.....	38
4.1. Optimization of intratracheal administration: Near infrared (NIR) FLI based tracking of Quantumdots .....	38
4.2. Pulmonary delivery of Auopolyplexes: in vivo tracking of siRNA by NIR fluorescence imaging.....	42
4.3. Monitoring CD49f targeted transgene gene delivery to breast cancer lung metastases by bioluminescence imaging.....	47
4.4. BLI within an immune-gene therapy approach by CD47 blockage and immune activation.	50
5. Conclusion.....	54
6. Appendix .....	56
6.1. QD FLI biodistribution data .....	56
6.2. Auopolyplex FLI and FLIT/CT biodistribution data .....	58
6.3. CD49f BLI and MRI.....	61
6.4. CD47 BLI .....	63
7. Summary .....	64

8. Zusammenfassung.....	65
List of abbreviations.....	66
References.....	68

## 1. Introduction

### 1.1. *In vivo* imaging

In accordance with the 3Rs (replace, reduce, refine) by Russel and Burch in 1959, *in vivo* imaging methods have become more and more important in biomedical research. The last three decades have seen an explosive growth in the number and applications of different imaging technologies (Condeelis and Weissleder 2010).

The main goal of *in vivo* imaging is to detect, localize and measure target molecules, pathways and physiology in a living subject (Smith and Gambhir 2017). With *in vivo* imaging it is possible to generate data non-invasively over a long period of time (several weeks and beyond) by using one and the same animal. This minimizes inter-individual variations resulting in more meaningful and comparable data. It is not only possible to get anatomical or physiological, but also functional information dynamically by using non-invasive methods (Smith and Gambhir 2017, Xu and Rice 2009). Repetitive studies of the same animals using different imaging assays at different time points can lead to dynamic and possible temporal assessments of therapeutic responses (Massoud and Gambhir 2003). Besides this, the ease of use of the diverse imaging devices and the rapid, high-throughput work is also a big benefit (Smith and Gambhir 2017, Xu and Rice 2009). Using less animals and getting lots of data out of every laboratory animal causes less costs (Massoud and Gambhir 2003). Especially when working with special transgenic- or knockout strains, where costs of several hundreds of euros per animal can arise, this is a benefit that has to be mentioned.

The diverse imaging systems can be grouped by different properties. First, they differ in the energy that is used to obtain the information (X-rays, photons, positrons, sound waves), the spatial resolution obtained (macro-, meso-, microscopic), or the type of information obtained (anatomic, physiological, molecular/ cellular) (Condeelis and Weissleder 2010).

For years, Computed tomography (CT) and magnetic resonance imaging (MRI) are in widespread preclinical and clinical use, both in humans and animals. On the other hand, Fluorescence imaging (FLI) and Bioluminescence Imaging (BLI), two molecular imaging approaches, are in experimental or preclinical use so far (Condeelis and Weissleder 2010). Each imaging modality has diverse benefits which justify its use in different projects or make a combination of different modalities necessary.

### 1.2. Magnetic resonance imaging (MRI)

Magnetic resonance imaging (MRI) is a tomographic imaging modality that gives excellent soft tissue contrast (Condeelis and Weissleder 2010). Despite the exquisite soft tissue contrast, the unlimited penetration depth is a useful property to show anatomical and pathoanatomical soft tissue fabric in its topographic surroundings (Busato et al. 2016). The underlying principle is that of Nuclear Magnetic Resonance (NMR). Here, the excitation and relaxation of atoms that are exposed to a strong magnetic field is measured (Busato et al. 2016). In MRI, these molecules are mostly protons within water molecules ( $H^+$  in  $H_2O$ ), so endogenous hydrogen nuclei with an inherent magnetic moment. Applying spatiotemporally varying magnetic fields leads to a disturbance of the steady-state. After perturbation, all nuclei relax by two unique and co-dependent relaxation mechanisms: T1 (spin- lattice relaxation) and T2 (spin- spin relaxation) (Condeelis and Weissleder 2010).

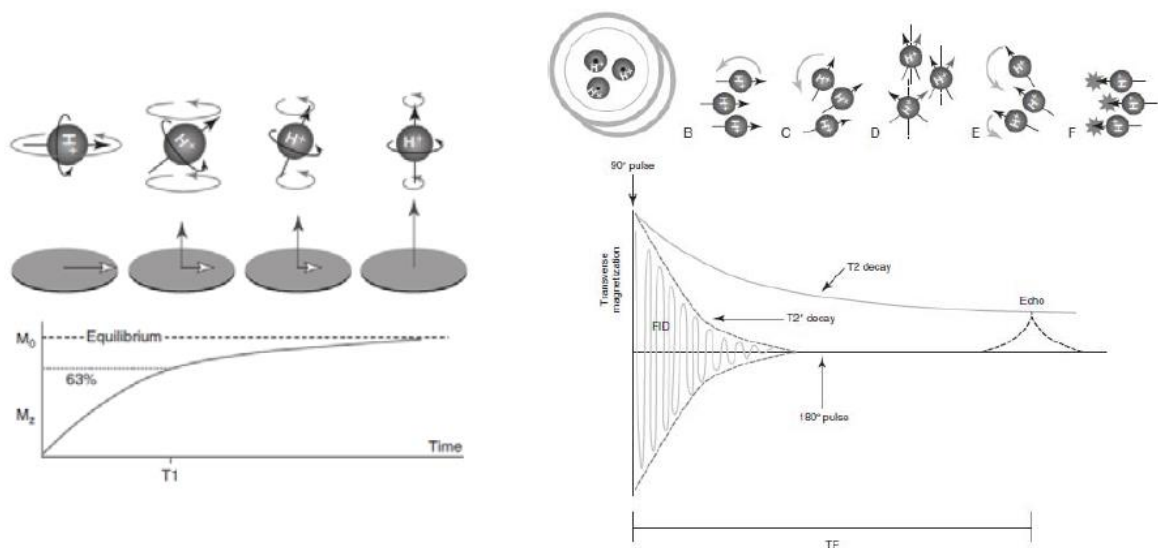


**Figure 1: Comparison of T1 and T2 weighted MR imaging mechanism;** (Thrall (2013): *Textbook of Veterinary Diagnostic Radiology*, 6th ed, p 62 and 63.)

By measuring these relaxations and the different relaxation times of the protons in tissues, the anatomical structures can be made visible. Nowadays, MRI is the most useful imaging modality in the detection and characterization of soft tissue pathology e.g. soft tissue tumors (Wu and Shu 2018).

### 1.3. Computed tomography (CT)

Computed tomography (CT) was the first tomographic imaging modality and used in clinical practice already from 1972 on (Kalender 2006). It is based on X-rays, a form of electromagnetic radiation with wavelengths from 10 to 0.01 nanometers (PerkinElmer 2012). This radiation is produced in a vacuum tube in which high energy electrons collide with a tungsten metal. Two atomic processes are able to produce x-rays: first there is the *bremsstrahlung*. Here, the high energy electrons emit X-rays when being rapidly slowed down due to interaction with the repulsive electron field of the tungsten metal. Second, x-rays can be produced by the high energy free electrons interacting with the atomic orbitals of the target metal (PerkinElmer 2012). The source of this radiation is then rotated around the object to be imaged, whereby many sectional images can be produced (Computed Tomography (CT), 2013). Computer calculation then leads to 3D images. In some CT devices not the X-ray source, but the object itself is rotating and sectional images are produced in this way (PerkinElmer 2012). When using x-rays, the soft tissue contrast, e.g. in comparison to MRI, is much less pronounced whereas dense structures, such as bones, can easily be made visible. To increase the soft tissue contrast, contrast agents can be used. These agents are highly radiopaque and can be injected i.v. or i.p. depending on the issue (Computed Tomography (CT), 2013).

Several contrast agents can be used for CT imaging. For example, iodine based ones are most commonly applied clinically, although several other, for example nanoparticulate ones, are applied in preclinical research (Lusic and Grinstaff 2013). Gold Nanoparticles or Auopolyplexes (AuNPs) hereby have different benefits compared to other materials. First it has to be mentioned that AuNPs, when compared to other polymeric micelles or liposomes, have much smaller sizes which is desirable for passive targeting of tumor tissues and reduced clearance (Chandran and Thomas 2015). They are non-toxic and have a high surface to volume ratio, which leads to enhanced binding properties and allows the conjugation of high numbers of ligands (Chandran and Thomas 2015, Rosi et al. 2006). Besides this, AuNPs are highly stable, have a high atomic number and X-ray absorption coefficient, which leads to high contrast in X-ray and CT-imaging when used as contrast agents (Chandran and Thomas 2015, Chen et al. 2018).

#### 1.4. Optical imaging

Another imaging modality is optical molecular imaging, which can be divided into fluorescence imaging (FLI) and bioluminescence imaging (BLI) (Wu and Shu 2018). The basic principle of optical imaging is the detection of photons emitted from the animal with a charged coupled device (CCD) camera and converting these photons to electrons for amplification (Youn and Hong 2012). Both, FLI and BLI reporter genes, are primarily used in mouse models of cancer. In combination with appropriate promoter or enhancer elements, such optical reporter genes can be expressed alone or as fusion proteins and allow longitudinal studies (Condeelis and Weissleder 2010). Therefore, BLI and FLI have great advantages for labelling and tracking of implanted cells as well as for the generation of transgenic reporter animals to be detected in distinct tissues or implanted tumors (Xu and Rice 2009).

#### **The optical imaging device**

An optical imaging device, such as the IVIS Spectrum CT *in vivo* imaging system (Perkin Elmer, Waltham, MA) (IVIS), is a gadget to induce (in case of FLI) and detect (BLI and FLI) light signals by means of optical imaging. In addition to these two kinds of optical imaging, it is also able to be used as a CT device. The high spatial resolution and strong penetration depth of CT make the combination of morphological imaging (CT) and molecular optical imaging highly beneficial (Wu and Shu 2018). The basic setup of an *in vivo* optical imaging device is a platform where the animal can be placed, an excitation light source for the FLI, a detector for the incoming photons, a so called charged coupled device (CCD), and a computer to process the obtained signals. The platform for the animals is heated to ensure a physiological body temperature of the animal while imaging. The platform also provides an apparatus for inhalation of anesthetics. The fluorescence excitation light source, in case of the IVIS a 150 Watt quartz tungsten halogen lamp with a dichroic reflector (Caliper Life Sciences 2007), is used to excite the fluorescent probes. The light can come from above or underneath the animal (more detailed information see [chapter 1.4.1.](#)). The detector for the incoming photons, a silicon chip of a CCD, is placed on top of the imaging device. The sensitivity of the camera is represented by the quantum efficiency (QE) (Welsh and Noguchi 2012). The photocathode releases free electrons caused by the incoming photons (Youn and Hong 2012). A computer then processes the data and converts these electron signals into a two-dimensional image (Sato et al. 2004). Afterwards

the software converts the different signal intensities into pseudo-color-scales to make the different intensity values easily visible for the operator (Zinn et al. 2009). The data themselves are still saved as photon- signal- strength, so no information is lost.

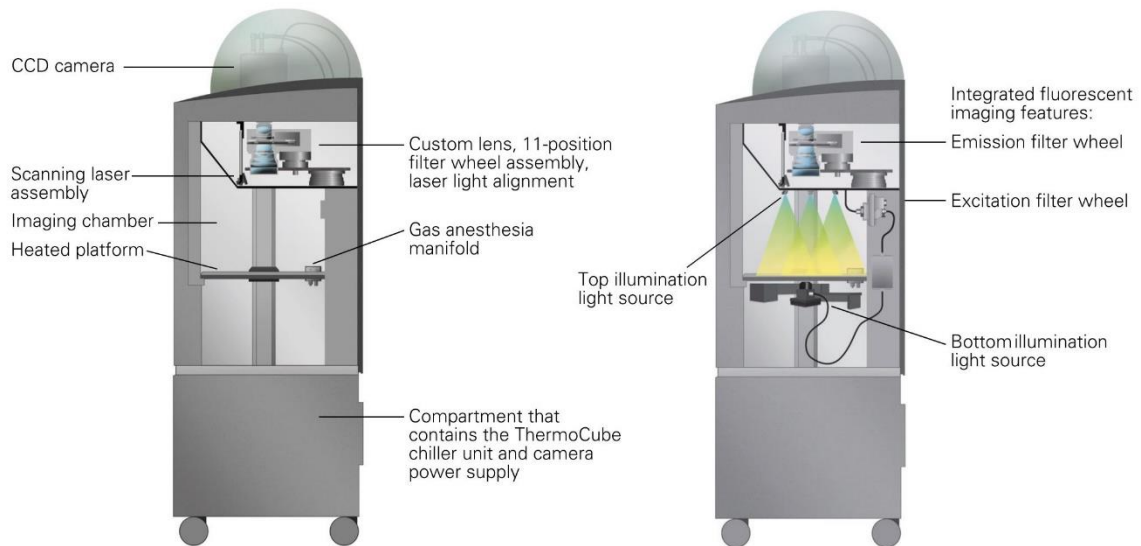


**Figure 2: Overview of the IVIS Spectrum CT.** (Caliper Life Sciences 2007)

A big problem in imaging is noise i.e. unwanted signals that have different origins. With an imaging device, like the IVIS spectrum, unwanted signals can be reduced in different ways and therefore increase the signal- to- noise- ratio. To avoid cumbersome and time consuming work steps, as described in some publications (e.g.(Welsh and Noguchi 2012) ) and to minimize disruptive light while imaging, the IVIS imaging chamber is a closed system and a completely light tight box (Sadikot and Blackwell 2005). The whole inside of the imaging chamber is made of non-fluorescing, non-bioluminescent and non-reflecting material. With these features it is assured that perturbing signals from the environment, the imaging chamber itself or reflections of the excitation light are set to a minimum (Caliper Life Sciences 2007).

The CCD is modified, too, to reduce noise from light as well as from its own background signal. To reduce the unwanted signals due to reflections of photons and to minimize signal loss, back-thinned CCD chips are used. These chips are transparent and illuminated from behind. Due to this way of construction photons have to penetrate less structures on the front of the chip. On the back of the chip there is also an antireflective coating which reduces signal loss due to reflection. With these CCD chips QE can often exceed 90% (Welsh and Noguchi 2012).

Not only photons can lead to noise in the imaging chamber. Emitted electrons from the CCD itself can lead to unwanted background signals, too. This effect is based on electrons that are constantly emitted from the CCD at higher temperatures and lead to the so called thermal noise (Keyaerts et al. 2014). These thermal electrons give rise to dark current (D) which is reported as electrons/pixel/sec (Welsh and Noguchi 2012).

To overcome this problem, the CCD is cooled to very low temperatures: by reducing the temperature, for every 7-8°C reduction the dark current is reduced by 50%. At a temperature of -90°C (this temperature is used in the IVIS due to combined thermoelectric water-cooling (Caliper Life Sciences 2007) values as low as 0.0001 electrons/pixel/sec are reached (Welsh and Noguchi 2012).

#### 1.4.1. Fluorescence imaging (FLI)

Even though tissue fluorescence was first noticed in 1852 its use for diagnostic purposes was recognized nearly 60 years later in 1911 (Andersson-Engels et al. 1997). Nowadays FLI seems to be one of the fastest growing imaging techniques (Condeelis and Weissleder 2010).

FLI systems need fluorescent probes, e.g. quantum dots, fluorescent dyes or reporter proteins, and an excitation light source which excites the fluorophore. This fluorophore then reaches a higher molecular level and by that emits photons of longer wavelengths (Wu and Shu 2018). This light signal then reaches the CCD camera after passing appropriate filters that are permeable for the fluorescence emission light (Rao et al. 2007).

In general, there are two models of fluorescence imaging ([Fig. 3](#)). The first one is based on epi-illumination. Here the reflected excitation light by a reporter group is detected. The excitation light source as well as the detector for the reflecting signal are on the same side of the animal. This method of fluorescence imaging is less time consuming, but signal strength decreases exponentially with the depth of the fluorescent source within the body (Leblond et al. 2010a, 2010b).

The second way to receive signals in fluorescence imaging is the transillumination mode. Here the excitation signal is on the opposite side of the animal than the detector for the emitted light. A benefit of this method is that signal strength is not affected much by the depth of the

fluorophores, the images contain more information and are more sensitive to fluorophores within deep tissue. However, it is more time-consuming than the epi-illumination mode and therefore does not allow a high throughput (Leblond et al. 2010a, 2010b).

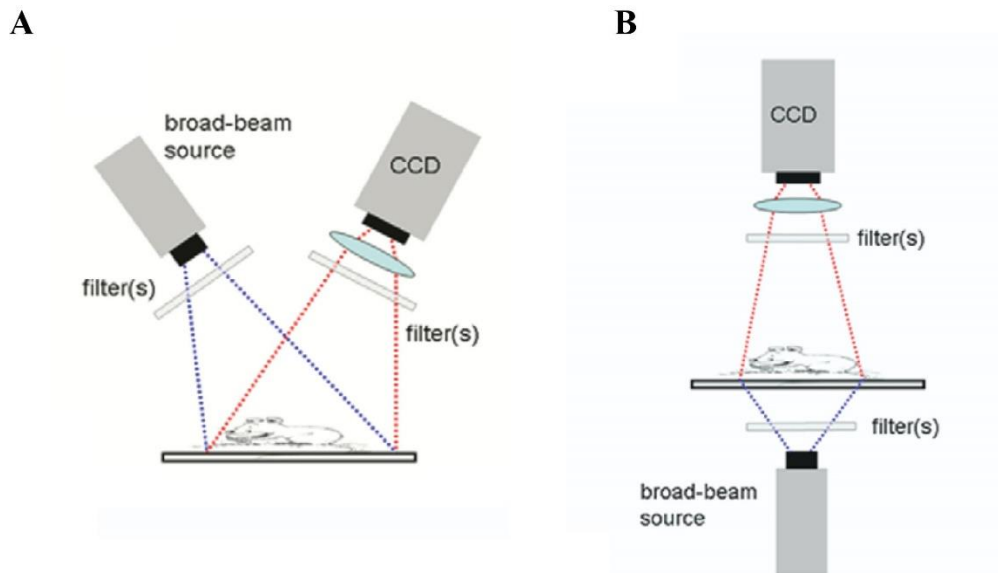


**Figure 3: Schematic comparison of Epi- (A) and Transillumination (B).** In Epi- Illumination the light source and CCD are on the same site whilst in Trans-Illumination they are on the opposite site of the animal; modified Leblond, Davis 2010

The specific signal detected by the CCD is always polluted by non-specific signals, so called autofluorescence, that originates from tissue, especially the skin, blood and hemoglobin, food components, excitation light leakage, unbound exogenous dyes or other contrast agents in the body (Leblond et al. 2010b). These noise-signals often cover up or corrupt the signals of interest, which makes different strategies necessary.

The strongest autofluorescence signal usually comes from the diet. Here the main factor for the fluorescent noise is alfalfa and chlorophyll, both parts of the normal lab rodent diet (Chul-Kyu and Hoonsung). The fluorescent excitation spectrum of chlorophyll is between 682 and 800 nm (Chul-Kyu and Hoonsung). Emission spectra of common, alfalfa- containing diet, often interfere with the range of NIR- or far-red imaging dyes. (Fig. 4) In this spectrum most of the FL measurements are done, which explains its high noise signals.

An easy and probably the most effective way to get rid of the autofluorescence in the 700 – 800 nm range caused by the food is by feeding a purified, low fluorescent diet. This diet is low in alfalfa and chlorophyll and therefore leads to less autofluorescence (Chul-Kyu and Hoonsung).

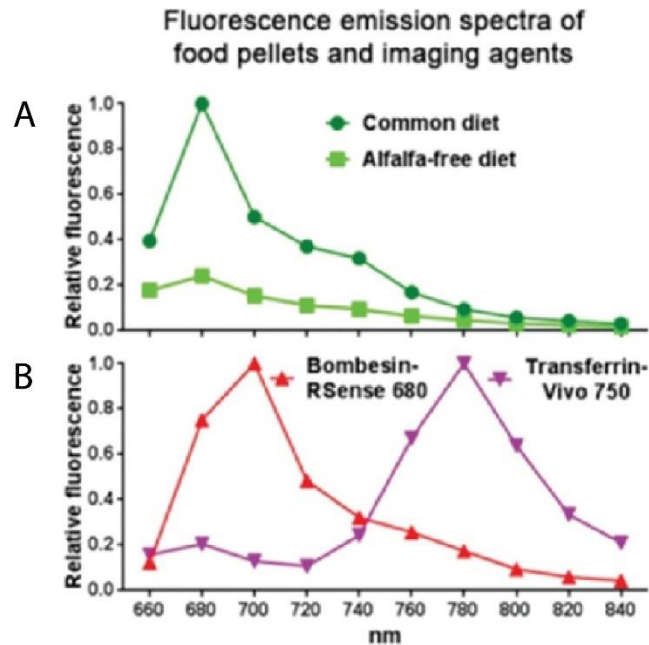


**Figure 4:**

*A: Fluorescence emission spectra of common diet and Alfalfa-free (low fluorescent) diet when using a 605 nm excitation filter. A clear peak is seen in 680 nm with the common diet whilst the low fluorescent diet has significant lower emission fluorescence; B: Two typical imaging agents in the NIR and far-red spectrum range, (PerkinElmer and Inc)*

Main absorbers of the fluorescent light, on the other hand, are hemoglobin, water and lipids. Their absorption rate is lowest in the region around 650- 900 nm, ([Fig. 5](#)) the near- infrared spectrum (NIR) (Resch-Genger et al. 2008, Shcherbakova and Verkhusha 2013, Weissleder 2001). This causes the tissue of the animal to be more transparent in the NIR (Shcherbakova and Verkhusha 2013). For this reason, using light in the NIR wavelength range can penetrate larger depths, up to several centimeters, with much less signal strength leakage which leads to better sensitivity (Leblond et al. 2010b, Ntziachristos).

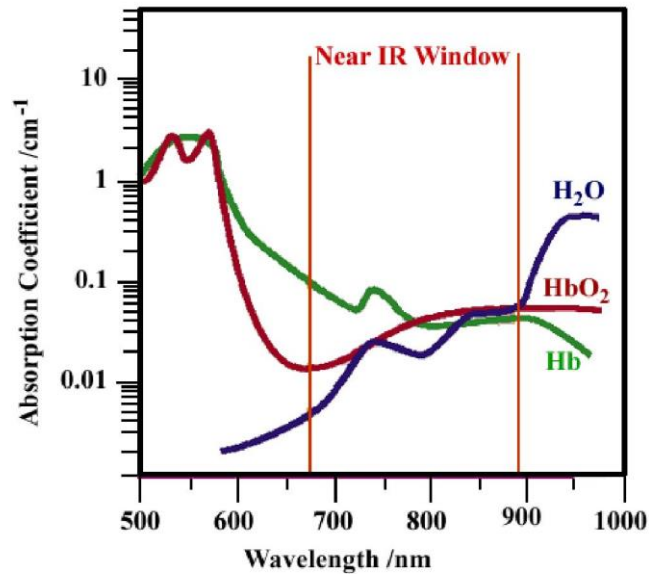


**Figure 5:** Comparison of the absorption coefficients of hemoglobin (Hb), oxyhemoglobin (HbO<sub>2</sub>) and water (H<sub>2</sub>O); the lowest absorption rate of all 3 components is in the range of 650 and 900 nm, the NIR window. (Bera et al. 2010)

Using a low fluorescent diet in combination with FLI reporters in the NIR spectrum is the best way to minimize autofluorescence and reach higher penetration depths. However, in FLI imaging there is always a background autofluorescence which can interfere with the true signals coming from the FLI reporters. This fact makes it inevitable to correct these unwanted signals.

By spectral unmixing it is possible to distinguish between the target fluorescence and the background autofluorescence. Moreover, contrast and sensitivity can be improved (Xu and Rice 2009). Nowadays these spectral unmixing techniques have been integrated into imaging systems and allow an easy processing of the images taken (Leblond et al. 2010a).

#### 1.4.1.1. Quantum dots (QDs) as near infrared (NIR) contrast agents

Quantum dots (QDs), also called semiconducting nanocrystals, are small inorganic materials normally in the diameter range of 1-10 nm (Mansur 2010). They mostly consist of an inorganic core (either core only or core-shell) and are coated with organic compounds for stabilization (Frangioni 2003). QDs can be used as nanocarriers being covalently or noncovalently attached to different types of drug carriers, e.g. liposomes or micelles, which enable their tracking in living tissue (Zintchenko et al. 2009). This is fostered by the high surface to volume ratio (Bera

et al. 2010). Using nano- carriers for drugs, in general, has different benefits such as smaller size, larger specific surface area, more and higher reactivity activity center and stronger absorption capacity (Zhao and Zhu 2016). When using nanomaterials as drug carriers there are different processes how these hybrids can enter cells: 1. Endocytosis, 2. Direct Microinjection (only with some cells), 3. Electroporation, 4. Mediated/ targeted uptake based on the nanomaterials surface (Mansur 2010).

QDs, compared to other nanomaterials, have several advantages. A big benefit, when working with QDs, is their size-dependent light emission and absorbance and a very large effective stokes shift (Fig. 6) (Ballou et al. 2005, Bera et al. 2010, Mansur 2010, Smith and Gambhir 2017). Nevertheless, QDs can be toxic due to their heavy metal coating (Mir et al. 2017). So diameters below 5.5 nm are required to ensure renal excretion and prevent accumulation in other organs like liver or spleen (Mansur 2010).

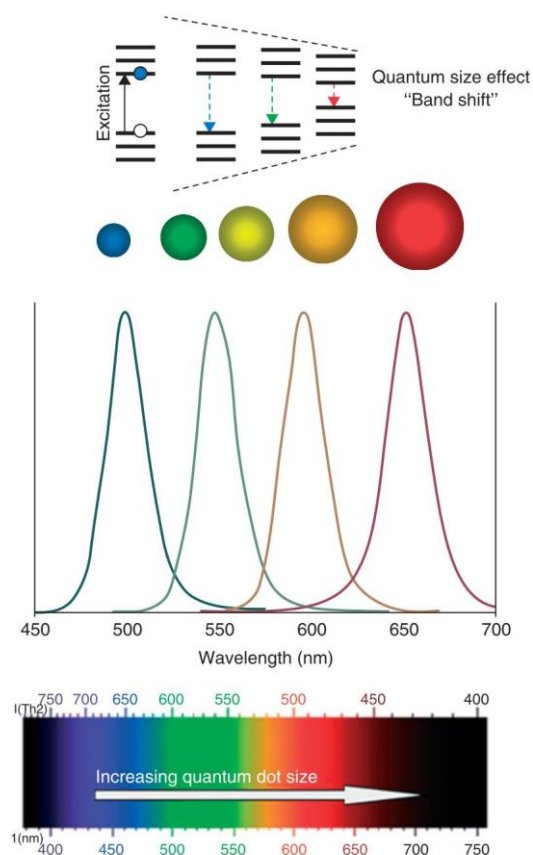


*Figure 6: Size dependent emission spectra of QDs (Mansur 2010)*

The absorption of QDs, in comparison to other organic dyes, increases indirect proportionally with the wavelengths (Chul-Kyu and Hoonsung, Resch-Genger et al. 2008). Using red- shifted near-infrared QDs can solve penetration issues in small animal imaging (Smith and Gambhir 2017). It has to be mentioned, that QDs have, due to their size, very narrow symmetric emission spectra, but broad excitation windows (Bera et al. 2010, Rao et al. 2007, Tan et al. 2014). A single light source is capable to excite multiple QDs with different emission spectra, so multiple fluorescence colors can be excited simultaneously (Rao et al. 2007). Other benefits of semiconductor nanocrystals compared to other organic dyes, is their high resistance to photobleaching (Bera et al. 2010, Frangioni 2003, Rao et al. 2007, Smith and Gambhir 2017, Tan et al. 2014). They have a relatively long lifetime from up to hundreds of nanoseconds (Bera et al. 2010, Resch-Genger et al. 2008). Besides this, QDs have a high quantum yield (Ballou et al. 2005, Rao et al. 2007). These circumstances allow imaging over longer periods of time which leads to good contrast by temporal discrimination of the signal of interest from background autofluorescence. These benefits explain the (perhaps) foremost usage of QDs in small animal fluorescence imaging since their introduction over a decade ago (Smith and Gambhir 2017).

#### 1.4.2. Bioluminescence Imaging (BLI)

In bioluminescence imaging, bioluminescent reporter proteins are used for imaging. These proteins are found in animals like the North American firefly (firefly luciferase, FLuc), click beetles (click beetle luciferase, CBR), the sea pansy *Renilla reniformis* (renilla luciferase, RLuc), and the copepod *Gaussia princeps* (Keyaerts et al. 2014). To be used as research tools, their genes have been cloned and genetically encoded as reporter genes (e.g. in cells, vectors etc.) inserted in cells or laboratory animals (Keyaerts et al. 2014). So far the majority of luciferases used are derived from beetles (Welsh and Noguchi 2012). The most commonly used luciferase reporter has its origin in the North American firefly *Photinus pyralis* (FLuc) (Badr and Tannous 2011, Noguchi and Golden 2017). This monomeric 61-kDa enzyme catalyzes the oxidation of its substrate, luciferin (Welsh and Noguchi 2012), and emits light with a wavelength of 530-640 nm with a peak at 562 nm (in the yellow- green spectrum). By using FLuc, imaging signals up to several centimeters deep within tissue can be detected, which makes it a good choice for detection of organs and growth of disseminated tumors (Sadikot and

Blackwell 2005). Besides this, due to its glow-type activity, it also produces a stronger and longer lasting signal when compared for example to the flash-like kinetic of renilla or gaussia luciferase (Sato et al. 2004). However the signal intensity decreases 10-fold with every centimeter of tissue penetration (Sato et al. 2004). Due to the short half-life of the FLuc protein in cells of about 3-4h it is a good choice for circadian studies (Noguchi and Golden 2017). The light itself is emitted during the enzymatic conversion of the substrate. (Fig. 7)

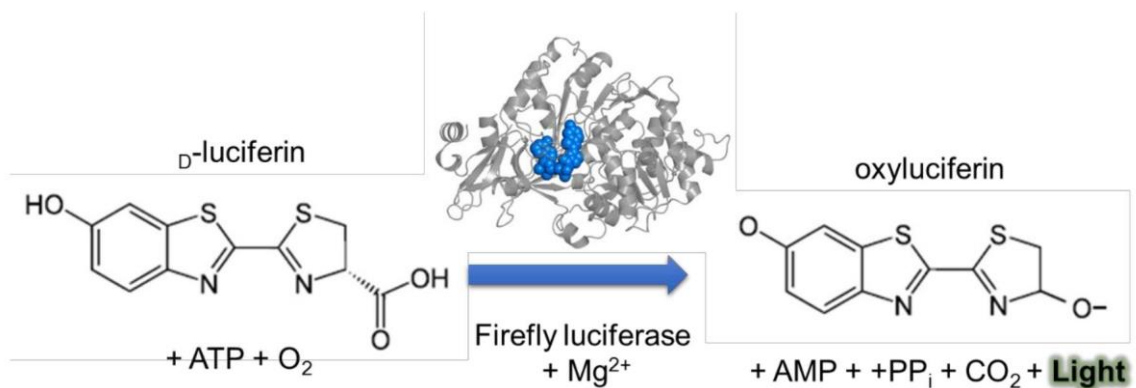


**Figure 7: Luciferin-luciferase reaction in firefly.** The light emitting reaction requires ATP, O<sub>2</sub> and D-luciferin. Mg<sup>2+</sup> and a luciferase catalyze the reaction. The output of the reaction is oxyluciferin, AMP, PPi, CO<sub>2</sub> and light. ATP: adenosine triphosphate, O<sub>2</sub>: oxygen; AMP: adenosine monophosphate; PPi: pyrophosphate; CO<sub>2</sub>: carbon dioxide (Noguchi and Golden 2017)

In this reaction O<sub>2</sub>, ATP, Mg<sup>2+</sup> and the exogenously administered substrate (luciferin) is needed. (Zinn et al. 2009). The enzyme luciferase then converts the substrate D-luciferin to oxyluciferin whilst releasing a photon (Keyaerts et al. 2014, Sato et al. 2004, Welsh and Noguchi 2012). The luciferin is usually injected intravascular or intraperitoneal (Sato et al. 2004). Subcutaneous injection is possible, too, if the expected signals are influenced otherwise.

The firefly luciferase was first cloned in 1985. Even though three years later it was already measured in mammalian cell lysates and showed its use for *in vivo* studies, it was not used in research for a long period of time due to its lower signal strength in comparison to FLI (Sadikot and Blackwell 2005). Nowadays BLI is the most commonly used optical imaging modality in small animals (Rabinovich et al. 2008). In BLI, auto-bioluminescence is also much lower than auto-fluorescence in FLI (Condeelis and Weissleder 2010). For this reason neither a low

fluorescent diet nor spectral unmixing is obligatory. Besides this, there are no excited photons that could interact with the bioluminescent signal. These incidents lead to much higher sensitivity and signal to noise ratio with BLI (up to 50x) in comparison to FLI (Welsh and Noguchi 2012). However, the drawback of this modality is that absolute signals are two to three log scales lower with FLI (Leblond et al. 2010b).

Another benefit of using BLI is the direct correlation of signal strength and tumor size/ number of viable tumor cells (Badr and Tannous 2011, Zinn et al. 2009). As described in a reported study, there is also a correlation between signal strength and number of metastases found in the organ (Sadikot and Blackwell 2005). On this occasion BLI has a sensitivity comparable to positron emission tomography (PET) and makes it a perfect choice for tracking tumor cells and for understanding the pathogenesis of metastasis *in vivo* (Sadikot and Blackwell 2005). This feature makes noninvasive, quantitative evaluation of tumor load before and after therapy fast and easy (Keyaerts et al. 2014). Several parameters, like fur, fur color, signal depth within tissue, imaging parameters itself and the diet, influence the BLIs sensitivity which has always to be kept in mind (Zinn et al. 2009). It is important to optimize these parameters. Besides the optimizations of instrumental parameters, like supercooling the CCD, other parameters as described in [chapter 1.4](#), e.g. the amount of luciferin injected can have a significant impact on the signal strength and therefore have to be standardized for each experimental setup. Even body temperature of the animal has an impact on light emission from the luciferase reaction. It decreases with lower body temperature, which makes it obligatory to ensure a physiological body temperature of the animal while imaging in anesthesia (Zinn et al. 2009).

When compared to FLI, BLI is the modality of choice for quantification purposes but lower spatial resolution a brightness restrict its use when precise localization in 2D of a signal is needed (Noguchi and Golden 2017, Welsh and Noguchi 2012).

#### 1.4.2.1. Tracking gene delivery efficiency- CD49f targeted polyplexes

CD49f, also known as  $\alpha6$ - integrin, is a transmembrane glycoprotein (Zhou et al. 2018). It is a biomarker commonly found on the plasma membrane of more than 30 different stem cell populations and even cancer stem cells (CSC), like breast CSC (Krebsbach and Villa-Diaz 2017, Zhou et al. 2018). Alternative splicing leads to two isoforms,  $\alpha6A$  and  $\alpha6B$ , which form heterodimers with  $\beta1$  and  $\beta4$  subunits (Zhou et al. 2018). Whilst  $\alpha6\beta4$  is commonly found in epithelial cells and stimulates the migration of carcinoma cells,  $\alpha6\beta1$ , besides other functions, promotes self-renewal of pluripotent stem cells and breast CSCs (Krebsbach and Villa-Diaz 2017, Mercurio et al. 2001, Zhou et al. 2018).

#### **PEG- coated nanoparticles**

The first line of defense on unprotected surfaces of the body, like the eyes, the respiratory-, the cervicovaginal- or gastrointestinal tracts is the mucus (Wang et al. 2008). Mucus protects these surfaces through its physiochemical properties, like pH, high viscoelasticity, pore size, ionic strength, charge and adhesivity against pathogens, toxins or ultrafine particles but can also minimize drug delivery to the underlying tissue (Leal et al. 2017, Wang et al. 2008). The thickness of the mucus layer depends on the localization. In the nasal cavity, for example, it has an immense thickness from up to 30  $\mu\text{m}$  whilst in the bronchi it is about 2-5  $\mu\text{m}$  (Leal et al. 2017).

In case of particle-based drug delivery, it is important for carrier particles to rapidly penetrate the mucus to avoid being shed and to increase its bioavailability (Wang et al. 2008). There are several ways to ensure a proper penetration of the mucus and to reduce opsonization, like capping the nanoparticles with e.g. polyethylene- oxide, poloxamer polysorbate, chitosan or gelatin (Chandran and Thomas 2015). Another way is to coat the nanoparticles with a high density of low molecular weight polyethylene glycol (PEG) ([Fig. 8](#)) (Liu et al. 2015).

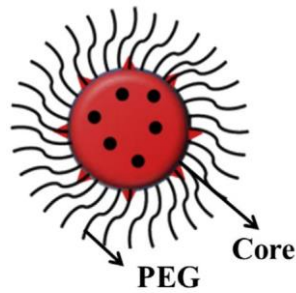


**Figure 8: Schematic PEG- Nanoparticle.** *With this PEG- coating the mucus can be penetrated more easily (Liu et al. 2015)*

This coating minimizes mucoadhesion by giving the nanoparticles a hydrophilic and near neutrally charged surface (Wang et al. 2008). It increases the particle transport rate up to 1100-fold depending on the particle size (Lai et al. 2007). Larger polymeric particles, with a size of around 500 nm, seem to have the best results here (Lai et al. 2007). Besides the effect of faster diffusion, the coating also adds stealth properties to the particles and enables a conjugation with other components (Kuzmov and Minko 2015, Liu et al. 2015). Even the non-specific deposition of the particles *in vivo* is reduced as well as molecular interactions and colloidal solubilities are improved (Ballou et al. 2005, Massoud and Gambhir 2003).

### **Linear polyethyleneimines (LPEIs)**

The negative charge, the instability as well as the molecular weight of RNA or DNA molecules prevent their crossing of membranes and their delivery (Höbel and Aigner 2013). This makes different strategies necessary for their protection against enzymatic and nonenzymatic degradation, their transfer through biological membranes and cellular uptake and their correct intracellular localization (Höbel and Aigner 2013).

In general gene delivery systems are classified into viral and non-viral systems. In comparison to viral systems, non-viral vector systems usually have a better safety profile. However, viral vectors can lead to higher transduction efficiency and long-term expression of the gene. Their drawbacks are immunogenicity, the risk of insertional mutagenesis, tumorigenicity, their limited delivery capacity and the high cost of production in a large scale (Zakeri et al. 2018).

Polyethyleneimine (PEI) is a cationic polymer and can be harnessed as a non-viral vector system. Initially, it was and still is used since many years in paper production, shampoo production and other technical applications. However, it was not introduced before 1995 as a versatile vector for gene delivery (Zakeri et al. 2018). These polymers are able to form stable nanoscale complexes with small RNAs (which are negatively charged) due to their positive charge (Castan et al. 2018, Höbel and Aigner 2013). By building those complexes the surface charge is masked or reduced (Kichler 2004). This leads to RNA protection, their cellular delivery via penetration and enhanced gene transfection (Castan et al. 2018, Höbel and Aigner 2013). The benefits of PEIs over other polycations such as L-Lysine are their high charge density, the so-called “sponge-proton effect” and chain flexibility (Zakeri et al. 2018). PEIs can be branched (BPEIs) or linear (LPEIs). A benefit of LPEIs over BPEIs is their lower cytotoxicity and increased transfection efficiency, which makes them an effective carrier for gene medicine, including DNA plasmids, small interfering RNAs (siRNAs) and mRNAs (Castan et al. 2018, Zakeri et al. 2018).

When combining PEI with PEGylation the biocompatibility is increased as well as the biological activity of the complexes. For example in intratracheal instillation PEG-PEI/siRNA complexes are way less toxic and more efficient for pulmonary induction of RNAi (Höbel and Aigner 2013, Kichler 2004).

#### 1.4.2.2. Tracking biological processes: tumor growth with CD47

Tumor cells can be marked with reporter genes enabling detection by bioluminescence. Due to the high sensitivity of BLI signals and an almost direct correlation of signal strength and tumor size, it is a good choice for tracking tumor growth and correlating metastases. The short half-life of luciferin (3-4 h) allows the imager to make longitudinal studies to track the tumor growth at several consecutive timepoints (Noguchi and Golden 2017).

In general, tumor growth is hindered by the innate and acquired immune systems. To escape immune surveillance and to obtain a tumor promoting microenvironment tumor cells developed several strategies. They can, besides numerous other strategies, recruit immunosuppressive cells or switch the phenotype and function of normal immune cells to function as tumor-promoting helpers (Liu and Cao 2016). Another strategy is to express transmembrane proteins

on their surface to mask their phenotype and therefore avoid attacks from the immune system. For example, cancer cell can protect themselves by expressing CD47 on their surface (Sherbet 2017).

CD47 (cluster of differentiation 47) is a transmembrane protein found on most body cells. The intercellular interaction of CD47 with SIRP $\alpha$ , another transmembrane protein expressed on cells of the immune system, can protect tumor cells by an anti-phagocytic signal to macrophages and dendritic cells (Sherbet 2017, Stanford Medicine 2018). Furthermore it regulates NO (Nitric oxide) and VEGF (vascular endothelial growth factor) signaling and therefore it is supposed to influence angiogenesis and metastatic spread (Sherbet 2017).

One option to re-activate the immune system to act against CD47 expressing tumor cells is hereby to block this surface protein with antibodies. This then allows macrophages to phagocytose the cells (Sherbet 2017, Takahashi 2018). The beneficial effects of the blockade of CD47-SIRP $\alpha$  interaction has already been shown *in vitro* and in several xenograft or syngeneic mouse models of cancer (Murata et al. 2018, Takahashi 2018).

For this reason, a novel gene therapeutic approach, namely the tumor-localized expression of the IL2- P- Fc protein after gene delivery into tumor cells, was developed in our lab (Billerhart et al, ongoing PhD thesis, manuscript in preparation). This fusion protein blocks the CD47 – SIRP $\alpha$  interaction and therefore inhibits the otherwise consistent “don’t eat me” signal. The IL2- part is needed for the secretion of the novel fusion protein after cytoplasmatic transcription to block the cell- cancer- cell interaction on the cell surface. The Fc- part, derived from immunoglobulin G (IgG), leads to an additional activation of the immune system.

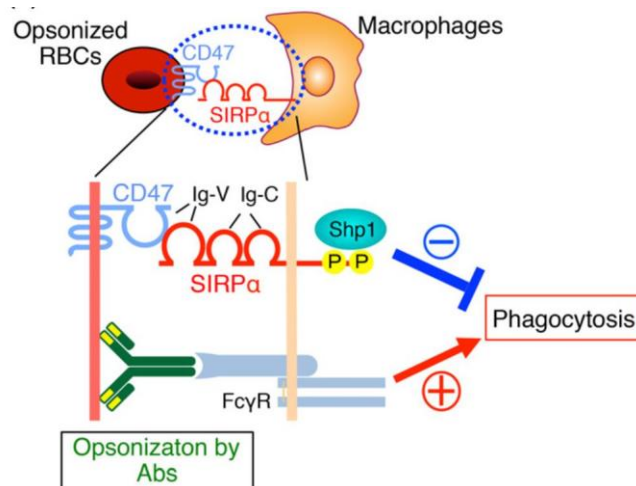


**Figure 9: Schematic opsonization of CD47-SIRP $\alpha$  interaction by antibodies.** This opsonization leads to phagocytosis of the RBCs by macrophages. The same mechanism is also present in tumor cells (Murata et al. 2018)

The underlying hypothesis of the CD47 project:

When using CD47 expressing cells/tumors (marked with firefly luciferase reporter gene for tracking growth in vivo by BLI) and treating them with a CD47 targeting therapeutic, IL2- P-Fc, tumor growth is affected. By measuring the BLI signal strength and in direct correlation the tumor size/ amount of viable tumor cells, the response to immunotherapy treatment of IL2- P-Fc can be detected. As a result, longitudinal studies allow the tracking of tumor growth and related biological processes.

### 1.5. Intratracheal instillation

The structure of the airways can be divided into the anatomical or conducting tract and the functional or respiratory tract. The anatomical tract primarily works as “transport” system for the air and has the function of heating the inhaled gases to physiological temperature as well as ensuring a non-harmful moisture. Besides this, the anatomical structures filter out potential toxic or otherwise pathogen particles. Here up to 90% of delivered drug particles are filtered (Patil and Sarasija 2012). Drug transport, controversially, is limited due to the relatively small surface and the lower regional blood flow. The anatomical tract can further be divided into nasal cavity, associated sinuses, nasopharynx, oropharynx, larynx, trachea, bronchi and bronchioles (Patil and Sarasija 2012). The larger airways are protected with a mucus layer. This mucus is secreted by goblet and submucosal gland cells and forms a hydrogel-like biopolymer barrier (Leal et al. 2017, Patil and Sarasija 2012). Together with ciliated cells, which promote upward transport of mucus, they clear the airways and lungs from foreign particles and substances (Patil and Sarasija 2012). This so called mucociliary system is the major clearance pathway in the larger airways (Grooneberg et al. 2003). The main task of the respiratory, functional parts is to ensure a proper gas exchange. This part consists of the respiratory bronchioles, the alveolar ductus and the alveolar sacs (Patil and Sarasija 2012). These smaller airways together with the alveolar space feature more than 95% of the airways surface. They are highly vascularized and directly connected to the systemic circulation via the pulmonary circulation (Patil and Sarasija 2012). This circumstance, together with morphologic conditions, like the thinness of alveolar cells, basement membrane and endothelial cells, ensure an adequate transepithelial transport of not only gases, but also of pulmonary applied drugs (Patil and Sarasija 2012). Like in the conducting airways, several barriers for foreign particles are existent in the lower airways. These barriers include surfactant in the alveolae, the phagocytic system (which is found all over the airways) and different transporters and enzymes (Feldmann and Merkel 2015, Geyer, Taschauer et al. 2017, Grooneberg et al. 2003, Kuzmov and Minko 2015).

When applying drugs or nucleic acids, there are different routes of administration like intravenous- (i.v.), intraperitoneal- (i.p.), intraoral (i.o.) or local, direct injection into the targeted organ. When injecting systemically (i.v., i.p. or i.o.) there is always the risk of having side effects and an increased accumulation in non-targeted organs, especially in liver, spleen or kidneys (Kuzmov and Minko 2015). Aggregation with serum proteins as well as degradation

by nuclease in the blood stream can decrease the therapeutic effect, especially when working with siRNA (Feldmann and Merkel 2015). In addition, the first pass metabolism with the risk of degrading the drugs to ineffective metabolites plays an important role as well as losing components in the gastrointestinal tract (Feldmann and Merkel 2015, Kuzmov and Minko 2015). This makes it necessary to apply higher dosages in order to achieve the desired concentration of the substance in the target organ.

In case of lung diseases, like asthma, chronic obstructive pulmonary disease, lung- cancer etc., local administration to the airways and targeting the lung tissue from the airway- side can prevent the shortcomings mentioned above (Feldmann and Merkel 2015).

To administer an aerosolized agent to the lungs, an exposure chamber can be used. This non-invasive technique enables to a good distribution of the applied drug within the lungs. Nevertheless, the disadvantages of this technique are that the exact dose reaching the lungs cannot be quantitatively controlled and larger amounts of the material are needed to obtain an adequate aerosol concentration. In addition, besides the lungs the whole animal surface is exposed to the agent, which can lead to safety issues when working with highly toxic materials (Bivas-Benita et al. 2005, Driscoll 2000).

To avoid whole animal exposure, reduce the drug dosage applied and to minimize the risk for the operator being exposed to toxic, radioactive or carcinogenic materials, intranasal or oral inhalative administration can be considered (Patil and Sarasija 2012). Whilst intranasal administration has several anatomical limitations (like narrower airway lumen leading to concentration losses of up to 85%), oral administration by inhalation can lead to far better results with concentration losses of only 20% (Patil and Sarasija 2012). The oral method can be categorized into intratracheal inhalation and intratracheal instillation. Here, the intratracheal instillation is the more commonly used method in small animal research (Patil and Sarasija 2012). A special syringe, a so called microsyringe, is inserted in the trachea and the material is administered via aerosolization (Driscoll 2000). The tip of the spraying device is placed slightly cranial of the *bifurcatio tracheae*. This ensures the administration directly to the lower airways without getting in contact with the respiratory dead space of the upper airways. Due to the small distance between the epithelial surface and the blood stream as well as the high vascularization, a fast absorption of the administered drugs can be achieved (Feldmann and Merkel 2015). This

application route enables a higher lung retention as well as good penetration and avoids accumulation in non-target organs (Patton and Byron 2007). Furthermore, the dosage applied can be tightly controlled and does not depend on the animals breathing frequency and breathing depth (Driscoll 2000).

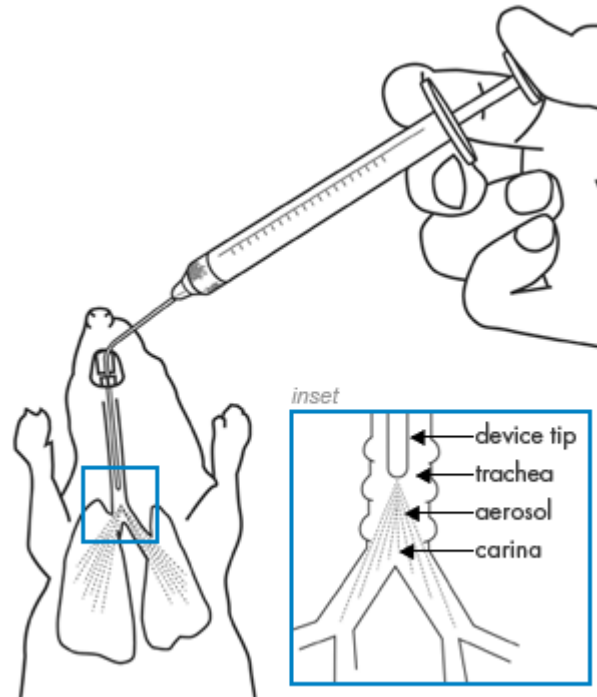


**Figure 10: Schematic intratracheal instillation with the PennCentury syringe.** To protect the trachea a 18G 1-inch catheter (B. Braun, Melsungen, Germany) is used. 04.04.2019 [http://penncentury.com/images/products/IA-1B\\_usediagram.gif](http://penncentury.com/images/products/IA-1B_usediagram.gif)

However, there are some disadvantages for this application method. First, the introduction of the syringe as well as the application of the high amount of a substance is not close to a physiological process. The total dosage of material administered and the rate of administration is far higher when compared with inhalation application. Furthermore, a physiological distribution of the instilled material within the respiratory tract cannot be ensured. In addition, the conducting, upper part of the respiratory tract is bypassed and potential interactions of the instilled material with these parts cannot be verified. Besides this, anesthesia is needed for this procedure, which could have an impact on the organism- drug- interactions (Driscoll 2000). The instillation directly cranial of the *bifurcatio tracheae* is the lowest accessible application

point. Still, the airways bifurcate 16-17 times before the alveoli area is reached (Patton and Byron 2007). This increases the risk of mucociliary escalation as well as losing parts of the formulation by coughing.

## 2. Aim of the Thesis

The overall aim of the thesis was to track nucleic acid-based drugs *in vivo* for studying biodistribution and transgene expression patterns by employing fluorescent and bioluminescent imaging to, respectively. Optical imaging was combined with X-ray absorption computed tomography to provide spatiotemporal information within three-dimensional imaging. In detail, the goals were as follows:

1. Optimize the intratracheal route of administration for quantum dots to follow the QD signal by near infrared fluorescence imaging in order to investigate the success of pulmonary delivery
2. Apply the optimized protocol for intratracheal aerosolization of Auopolyplexes (gold nanoparticle formulation loaded with siRNA)
3. Apply targeted gene delivery polyplexes into CD49f overexpressing lung tumor lesions in a 4T1 murine triple negative breast cancer model and track firefly luciferase reporter gene expression via bioluminescence imaging.
4. Monitor tumor growth by bioimaging in an immune-gene therapy approach by implantation of luciferase expressing MDA-MB-231 cells and treating them with polyplexes

### 3. Materials and methods

#### 3.1. Animals

All animals used for experiments were housed in individually ventilated cages (Type 2L; Tecniplast, Hohenpeißenberg, Germany) under specified pathogen free conditions and a 12/12 light/dark cycle at a constant temperature of 21 degrees and a humidity of 60%. The animals were allowed to acclimatize for at least ten days prior to experiments. Autoclaved water and food (standard rodent diet; SSniff, Soest, Germany) was provided *ad libitum*. Low fluorescent diet (BROGAARDEN D10001 AIN-76A; Korn & Foderstoffer ApS, 3540 Lyngø, Denmark) was fed for at least ten days prior to the experiments. All animals were shaved ventrally and dorsally with an Aesculap clipper (Isis Aesculap®, B. Braun, Buchbach, Germany) right before imaging to improve the signal quality. By administration of an eye ointment (VitA POS® Eye ointment with retinol palmitate, Ursapharm, Saarbrücken, Germany) protection of the eyes was ensured during anesthesia.

The mice were controlled daily for changes in body weight, mobility and activity. Mice were euthanized if tumor progression impaired their mobility or wellbeing, more than ten percent of their body weight was lost or the mouse appeared to be in other forms of distress. Relevant data regarding the animals (e.g. imaging procedures, welfare and body weight) were documented in the Animal Facility Software PyRAT (Scionics Computer Innovation GmbH, Dresden, Germany).

In the QD- project 8 mice (BALB/cJRj, with specific- pathogen- free (SPF) quality, female; purchased from Janvier Labs, Le Genest-Saint-Isle, France) aged 33 to 73 weeks were used. After intratracheal instillation of the QDs the animals were imaged by 2D FLI and 3D FLIT/CT in supine and prone positioning and a second time 24h thereafter. Afterwards, animals were sacrificed by cervical dislocation, organs were imaged *in situ* and *ex vivo* by 2D FLI and thereafter frozen in TissueTek® cryomedium using appropriate molds.

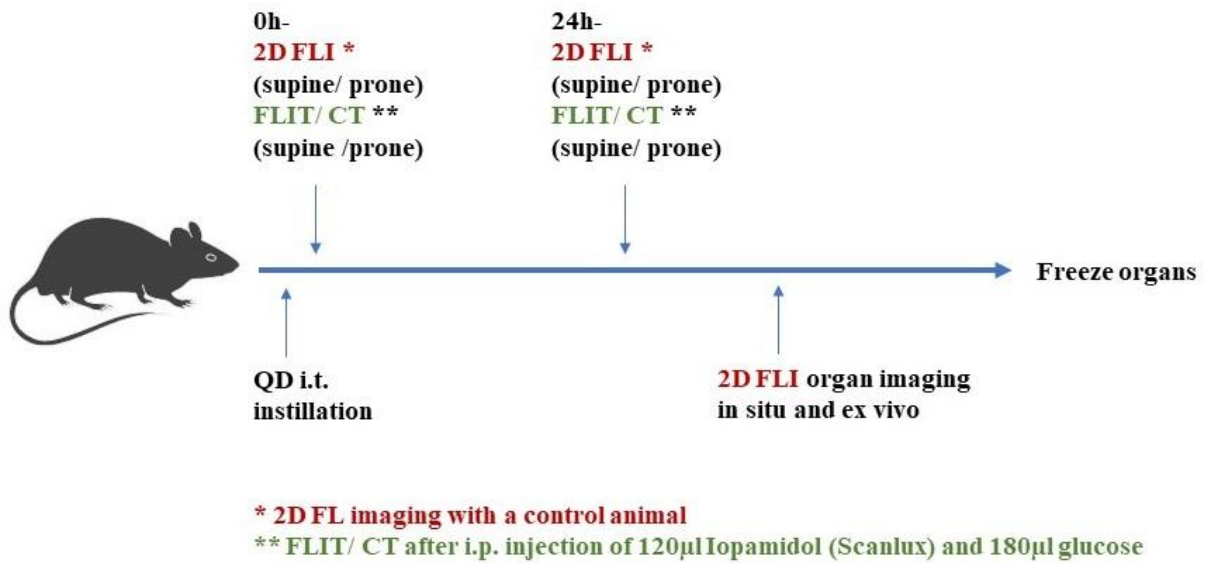


**Figure 11:** Timeline of the QD project. 8 female BALB/cJRj mice were intratracheal instilled with QDs and imaged immediately after application (0h) and 24h thereafter (24h) with 2D FLI and FLIT/CT in supine and prone positioning. After the 24h imaging time point, animals were sacrificed, organs imaged in situ and ex vivo with 2D FLI and the frozen in TissueTek®.

For the AuNP- project, 13 mice (BALB/cJRj, with SPF quality, female; purchased from Janvier Labs, Le Genest-Saint-Isle, France) aged 35 to 89 weeks were used. After intratracheal instillation of the Auropolyplexes, the animals were imaged by 2D FLI and 3D FLIT/CT in supine and prone positioning. 24h after instillation the animals were imaged a second time. Afterwards, animals were sacrificed by cervical dislocation, organs were imaged in situ and ex vivo by 2D FLI and thereafter frozen in TissueTek® cryomedium using appropriate molds.

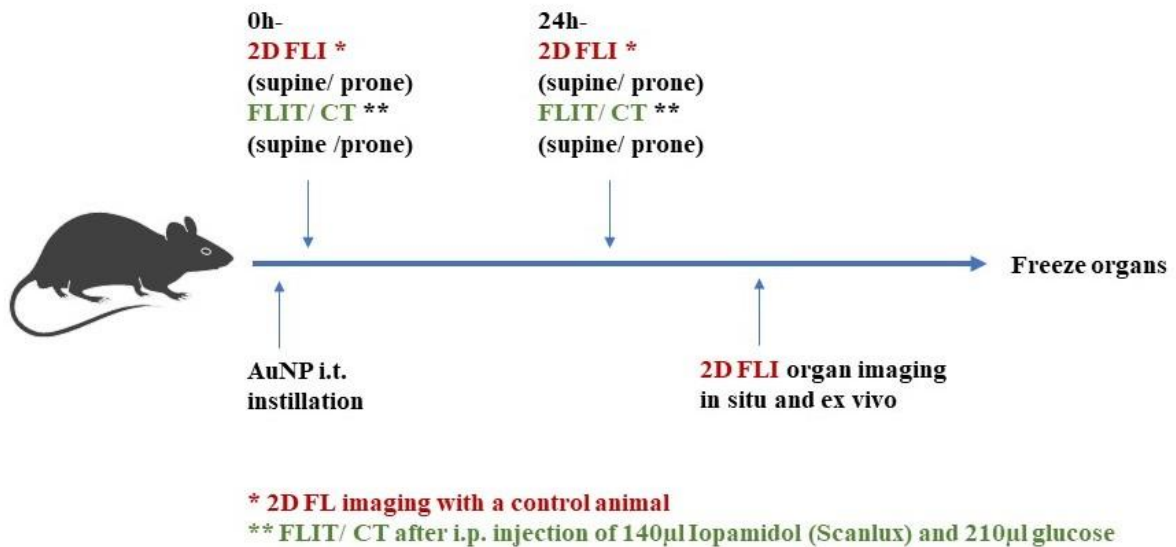


**Figure 12:** Timeline of the AuNP- project. 13 female BALB/cJRj mice were intratracheal instilled with AuNPs and imaged immediately after application (0h) and 24h thereafter (24h) with 2D FLI and FLIT/CT in supine and prone positioning. After the 24h imaging time point, animals were sacrificed, organs imaged in situ and ex vivo with 2D FLI and then frozen in TissueTek®.

For the CD49f- project 30 mice (BALB/cJRj, with specific- pathogen- free (SPF) quality, female; purchased from Janvier Labs, Le Genest-Saint-Isle, France) aged 14 - 29 weeks have been used. 4T1- iRFP720 human breast cancer cells were harvested, washed and resuspended in DPBS ( $10^6$  cells/mL). Animals were on a low fluorescent diet for at least 10 days prior to tumor cell implantation. Cells were injected i.v. into the lateral tail vein ( $10^5$  4T1-iRFP720 cells per injection). On day 10 or 11 animals were imaged by MRI and in 2D FLI. When tumor growth in the lung parenchyma was identified by MRI, the animals were treated with PEG- or CD49f polyplexes via the intratracheal route and were imaged afterwards in 2D FLI in supine and prone positioning. 24h afterwards the animals were imaged in 2D FLI and 2D BLI in supine and prone positioning before their lungs were fixated via formaldehyde instillation.

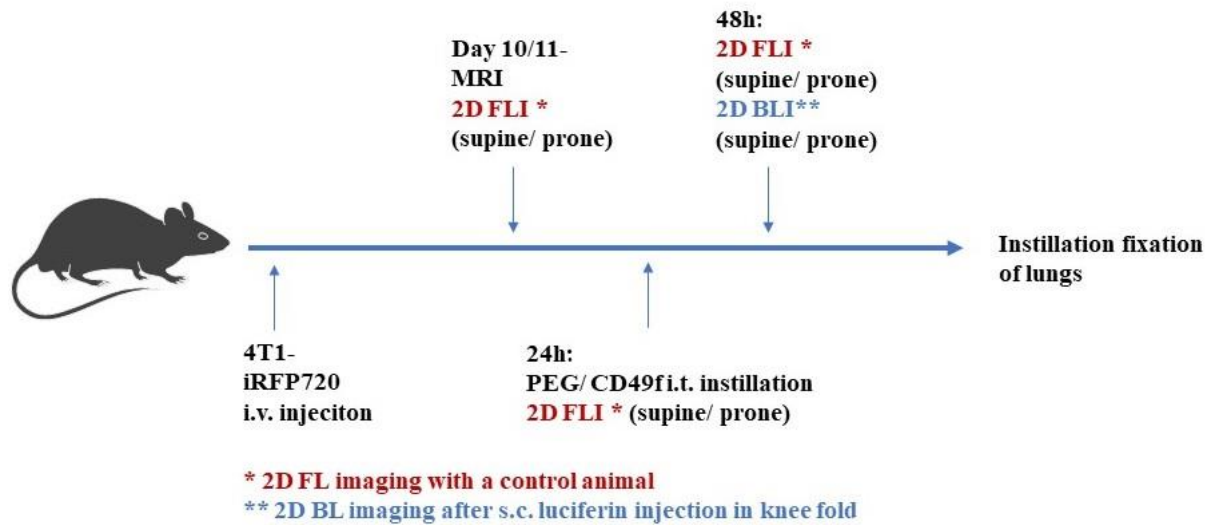
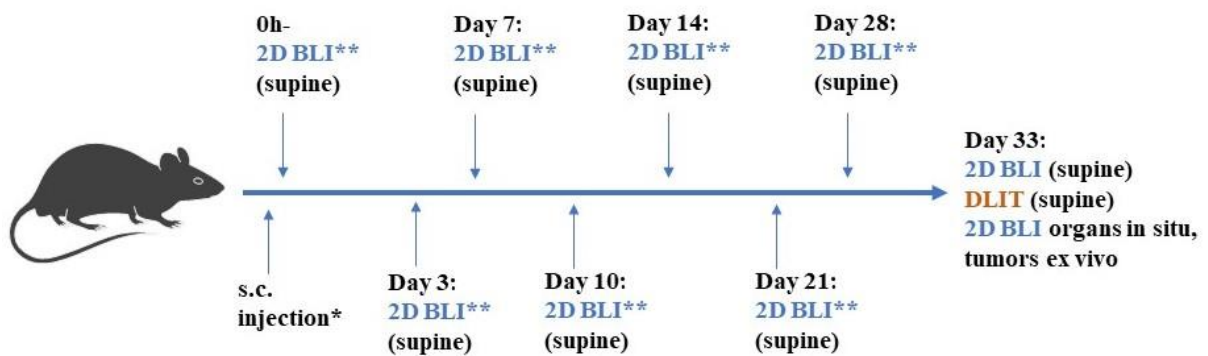


**Figure 13:** Timeline of the CD49f project. 30 female BALB/cJRj got 4T1-iRFP720 injection in the lateral tail vein. 10/11 days after injection the tumor load was imaged with MRI followed by 2D FLI in supine and prone positioning. 24h after the first imaging the animals were treated with PEG (as a control) or CD49f via the intratracheal route. 48h after instillation the animals were imaged in 2D FLI and 2D BLI in supine and prone positioning. Afterwards the lungs were fixated via formaldehyde instillation.

In the CD47 project, 9 female CB17 severe combined immunodeficient (SCID) mice (with SPF quality, purchased from Janvier Labs, Le Genest-Saint-Isle, France) aged to 36 weeks were used. These mice lack functional T- and B- cells and therefore also immunoglobulins, so these components of the adaptive immune systems cannot interfere with the tumor cells or the injected substrates and the mice can host tumor cells from different species, in this case tumor cells from human origin. By using SCID mice in this project we can focus on actions of the innate immune system. After setting the animals on a low fluorescent diet, a subline of the triple negative breast cancer cell line MDA-MB-321, namely 231/LM2-4 (Munoz et al. 2006) was used, which exhibits faster growth *in vivo* when compared to the parental line.  $1 \times 10^6$  231/LM2-4 -EGFRLuc human breast cancer cells (3 animals per group) were injected percutaneously in the region of the mammary fat pad of the 4<sup>th</sup> glands complex. As the cells were also genetically marked to express a fusion protein of firefly luciferase and enhanced green fluorescent protein, their growth could be monitored *in vivo* by BLI. Cells were transfected with polyplexes containing plasmid IL2-P-Fc, which encodes a secreted fusion protein of a SIRP $\alpha$

domain and the Fc part of human IgG (immune-gene therapy), or the plasmid bb-mCherry encoding for the red fluorescent reporter protein mCherry (transfection control) or were left untransfected (as unstained control). Directly after transfection the animals were imaged with 2D BLI in supine positioning. On days 3, 7, 10, 14, 21 and 28 after s.c. injection the animals were imaged in 2D BLI in supine positioning to track tumor growth. On day 33 the animals were imaged in 2D BLI and DLIT in supine positioning. After sacrificing the animals, tumor and organs were imaged *in situ* by 2D BLI.



\* s.c. injection in the region of the mammary fat pad (4<sup>th</sup> glands complex); Groups: IL2-P-Fc, bb-mCherry control, untransfected control  
 \*\* 2D BL imaging after s.c. luciferin injection in the neck

**Figure 14:** Timeline of the CD47 project. In total 9 female CB17 SCID mice were injected with IL2- P-Fc or bb-mCherry (control) polyplexes or left untransfected (unstained control) MDA-MB-231 cells s.c. in the region of the 4<sup>th</sup> mammary fat pad. To track tumor growth animals were imaged 7 times in the following 28 days with 2D BLI in supine positioning. On day 33 the animals were imaged in 2D FLI followed by DLIT. After sacrifice 2D BL organ imaging and tumor imaging *ex vivo* was conducted.

All procedures were approved by local ethics committee and are in accordance with the Austrian law for the protection of animals and the EU directive 2010/63/EU for animal experiments. (BMWFV-66.006/0027-WF/V/3b/2014; 17.10.2014; last changed: BMWFW-66.006/V/3b/2018 ,19.01.2018)

### 3.2. Intratracheal instillation

Within the QD, the AuNP and the CD49f project the reagents were applied into the lung by intratracheal instillation. The mice were anesthetized by Ketamine/ Xylazine (80mg/kg and 5mg/kg) via intraperitoneal injection and, after reaching an adequate depth of anesthesia, placed on an inhouse made intubation platform. Mice were intubated with an 18G 1 in. catheter (B. Braun, Melsungen, Germany) and the formulation was administered intratracheally by using the MicroSprayer®/Syringe Assembly (MSA-250-M, Penn-Century, Inc.; Wyndmoor, PA, USA). The syringe was placed right above the tracheal bifurcation to enable direct and equal delivery into all lobes of the left and right lung. A gooseneck lightguide with a white LED was placed ventrally and slightly cranial of the *apertura thoracica cranialis* to secure a proper intratracheal positioning of the tube. After application, animals were held with head up to minimize the risk of coughing and to prevent the liquid applied to be swallowed and reach the gastrointestinal tract. Thereafter, mice received 140 µl Iopamidol (Scanlux, Sanochemia, Vienna; 300 mg iodine/ml) in 5% glucose (in a ratio of 1:1.5 (Iopamidol : 5% w/v glucose) i.p. and were scanned on an IVIS Spectrum CT imaging system (PerkinElmer, Waltham, MA 02451, USA) (Geyer, Lorenzer et al. 2017).

Details of QD formulation used for optimization of intratracheal administration: CdTe quantum dots (capped by mercaptopropionic acid; 720nm emission maximum) were prepared in HBG buffer by taking 41.6µl of QDs (batch1) and adding 58.4µl HBG to get 100µl. 75µl of this formulation was used for intratracheal administration.

Details of Auropolyplexes used for siRNA tracking in vivo:

75µl of Auropolyplexes containing a total of 10 µg of ALSL10 Auropolyplexes with AF750-siRNA in HBG was applied (133µg/ml). For more details on Auropolyplex formulation, please refer to the following manuscript (Taschauer et al. 2019) and thesis titled ‘Synthesis of auropolyplexes and their biophysical evaluation (Stefan Pöschl)’.

Details of polyplex formulation used for CD49f targeted gene delivery:

Preparation of polyplexes was conducted based on a previously described method. (Rödl et al. 2013) Polyplexes were prepared by mixing plasmid DNA (pDNA for firefly luciferase reporter gene) with either targeted version of LPEI (LPEI-PEG-CD49f) or non-targeted PEG control

(LPEI-PEG) by flash pipetting at a final pDNA concentration of 267  $\mu\text{g}/\text{mL}$ . The mixture was then incubated for 5 minutes at room temperature. 75 $\mu\text{l}$  of polyplex solution (N/P 9 in HBG, day 11 *postimplantationem* of 4T1-iRFP720 cells, LPEI/ LPEI- PEG/ LPEI-PEG-CD49f polyplexes) were administered.

### 3.3. Imaging

Animals were anaesthetized with isoflurane in an induction chamber at an initial setting of the vaporizer at 5%.

After reaching an adequate depth of anesthesia, the further handling and imaging was maintained with 1,5- 3% Isoflurane in oxygen (FiO<sub>2</sub> = 100%) as a carrier gas (2l/min). Anesthetized animals were placed on a heating plate (40° C) to ensure a physiological body temperature. Within extended imaging sessions and to ensure a better recovery for animals with a more heavy tumor load, 500µl 5% Glucose (B.Braun, Melsungen, German) was administered intraperitoneally.

Prior to BLI imaging, animals received D- Luciferin (D- Luciferin potassium salt, Intrace Medical SA, Lausanne, Switzerland) by subcutaneously injection within the neck region, which should ensure optimal signal detection (Inoue et al. 2009). D- Luciferin was dissolved in DPBS at a concentration of 30 mg/ml and applied at a dose of 120 mg/kg.

The optical imaging (BLI, FLI and FLIT) was performed by using the IVIS Spectrum CT in vivo imaging system (Perkin Elmer, Waltham, MA).

Analysis was done by spectral unmixing in Living Image Software (IVIS Spectrum Series, version 4.5.2.18424). For the evaluation of light signal a region of interest (ROI) was placed over the active region.

#### QD and Auropolyplex experiment:

All animals were imaged by 2D fluorescence imaging with the following Excitation (Exc.) and Emission (Em.) filter settings: Ex 640nm with Em 680 nm, 700 nm, 720 nm, 740 nm, 760 nm; an Ex 675 nm with Em 720 nm, 740 nm, 760 nm, 780 nm and 800 nm. Treated and untreated reference animals were imaged side- by- side (Stage C) to ensure a proper background subtraction. After imaging the animals in 2D, the animals received 300µl of a 1:1.5 mixture of Iopamidol [300mg iodine/ml] (Scanlux®; Sanochemia; Vienna) with 5% glucose i.p. as CT contrast agent for the following 3D imaging. The 3D FLIT/CT imaging was done in transillumination mode at an Excitation filter setting at 675 nm (30 nm BW) and an Emission filter setting at 720 nm (20 nm BW).

After 24 hours, animals were imaged again in 2D FL and 3D FLIT/CT as described above. Afterwards the animals were sacrificed by cervical dislocation during isoflurane anesthesia followed by an organ imaging by 2D FL in stage B.

#### CD49f experiment:

Prior to imaging, 4T1-iRFP720 cells (murine triple negative breast cancer cell line stably transduced to express the reporter gene iRFP720 (Geyer, Taschauer et al. 2017) were injected i.v. into the lateral tail vein.

The animals were placed on an inhouse made platform to combine magnetic resonance tomography and optical imaging. Monitoring of tumor growth was conducted with a 1,0 Tesla Aspect Imaging® M3 compact MRI system (Aspect Imaging, Shoham, Israel) equipped with a 50 mm x 30 mm body coil (time to repetition: 3250 ms; time to echo: 63.47 ms; number of slices: 15; slice thickness: 1 mm; number of excitations: 7; slice orientation: coronal; center of slice position: 0; flip angle: 90°; scan time: 5 minutes 46 seconds). A significant tumor load in the lung detectable by MRI was taken as major criterion for starting the treatment. After imaging the animals with MRI, 2D FLI imaging was conducted with following settings:

Ex 640 nm with Em 680 nm, 700 nm, 720 nm, 740 nm, 760 nm; Ex 675 nm with Em 720 nm, 740 nm, 760 nm, 780 nm and 800 nm and Exc. 710 nm with Em 760 nm and 780 nm.

When tumor size allowed a treatment, i.t. application of polyplexes was performed as described above. 24 h after treatment animals were imaged with MRI and in 2D BLI. After injection of luciferin, the bioluminescence signal was collected within a time series at an exposure of 5 minutes in Stage B with above described filter settings over a duration of 30 – 45 minutes until a peak in the signal strength was clearly visible.

#### CD47 experiment:

Animals were imaged for a time period of 33 days.

After injection of luciferin, all animals were imaged by 2D BLI (setting with open emission and blocked excitation filter) in a time series with exposure times of 3 minutes. All 3 animals from one group were imaged at the same time in stage D and in supine positioning. When a peak in

the signal strength was clearly visible, the animals were covered and every animal was imaged alone in stage B with the settings mentioned above. On the last imaging day, all animals were imaged alone in stage B and supine positioning. Afterwards 3D FLIT measurement was performed with following settings: Emission: 560 nm, 580 nm, 600 nm, 620 nm, 640 nm and Excitation: Block. After cervical dislocation during isoflurane anesthesia, all organs were imaged *in situ* and *ex vivo* using above-mentioned 2D BLI settings.

## 4. Results and discussion

### 4.1. Optimization of intratracheal administration: Near infrared (NIR) FLI based tracking of Quantumdots

Intratracheal administration was optimized by employing near infrared fluorescence imaging to decipher the success of pulmonary delivery (microspraying) of quantum dots into mice by following the QD signal. Up to 75 $\mu$ l of the QD containing solution was applied via intratracheal instillation with the Penn Century sprayer as described in the i.t. section (3.2). This amount was well tolerated by the animals and they showed no signs of respiratory distress. After i.t. delivery epifluorescence imaging was performed as described in the imaging section (3.3) and according to the technical notes released by PerkinElmer. For image analysis the “manual spectral unmixing process” was used. This tool distinguishes between background signal and AF750 signal (with excitations of 675 nm and 725 nm) by deducting the calculated mixed autofluorescence/AF750 signal for each pixel.

After applying the QDs and imaging the animals immediately after instillation, a strong signal was observed in the thoracic area in prone as well as in supine positioning. (Fig. 15) This indicates the successful application of the QDs in the lung. Due to the intratracheal application route faint signals can be observed in the trachea in some animals as shown in Figure 15 B.

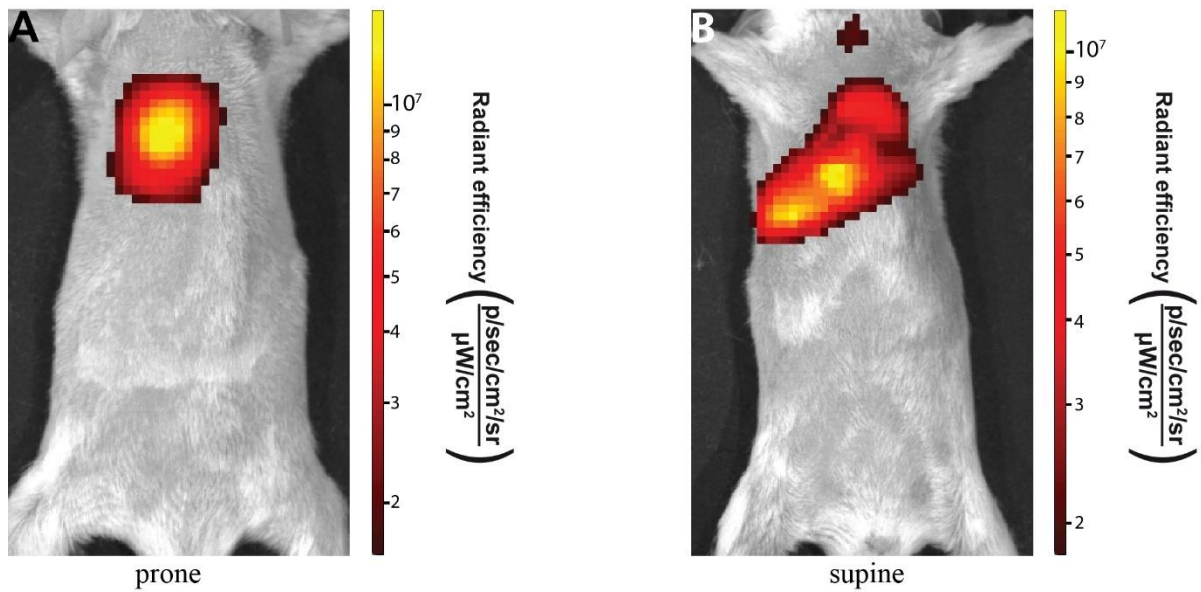


**Figure 15: 0h 2D epifluorescence imaging of Quantumdots after intratracheal pulmonary delivery.** Female BALB/cJRj mice were treated with quantumdots intratracheally and imaged immediately after application in prone (A) and supine (B) position. In both positions a strong signal is observed from the thoracic area indicating a successful application in the lungs. Color coded fluorescence radiance images are overlaid onto reflected light images.  $n=3$ , representative animals are shown.

Animals were imaged a second time 24h after instillation. Hereby a strong signal remained visible in the thoracic area when imaged in prone positioning. (Fig. 16 A) In some animals a signal was also found in the abdominal area in the region of the stomach when imaged in supine positioning. (Fig. 16 B) However, these signals were 10-fold lower than the signals detected in the thoracic area and may result from coughing up and swallowing small proportions of the i.t. applied liquid.

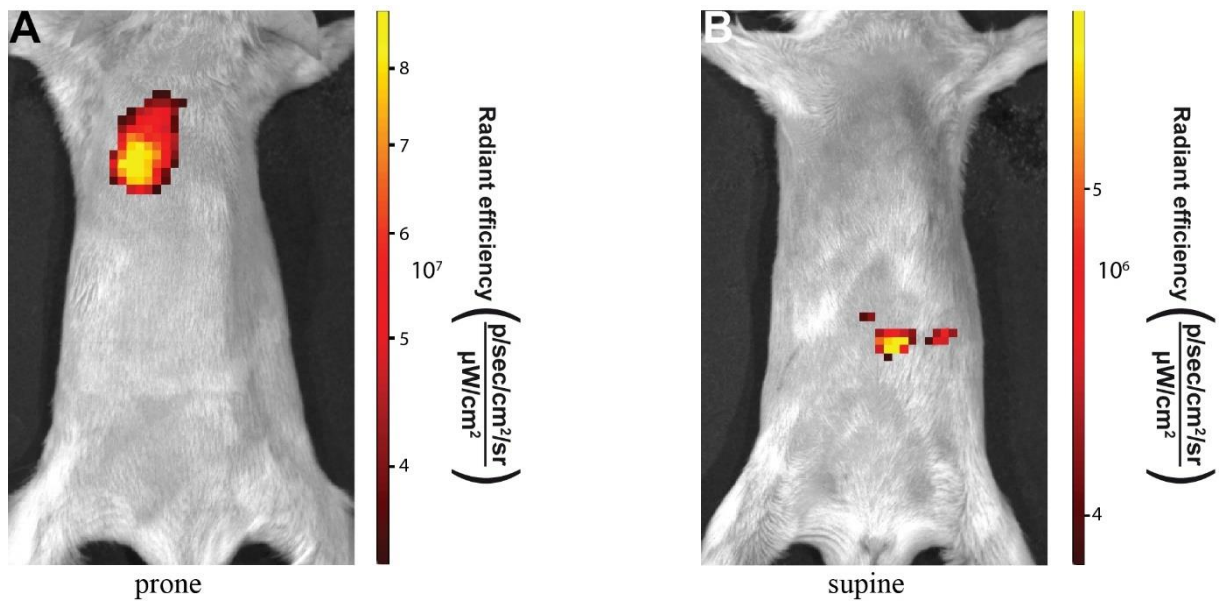


**Figure 16: 24h 2D epifluorescence imaging of quantumdots after intratracheal pulmonary delivery.** Female BALB/cJRj mice were treated with quantumdots intratracheally and imaged 24h after application in prone and supine position. In prone position a signal is observed in the region of the lungs. In supine position only slight signals coming from the abdominal area are observed indicating swallowing of small amounts of the instilled material. Color coded fluorescence radiance images are overlaid onto reflected light images. ( $n=3$ , representative animals are shown.)

Because exact allocation to anatomical sites can be difficult using 2D-FLI, animals were sacrificed by cervical dislocation after the second imaging and the organs were imaged in 2D FLI *ex vivo*. Hereby the strongest signal was obtained from the lungs. (Fig. 17) In some animals a faint signal was also obtained in the stomach which confirmed the findings in 24h whole animal imaging. These signals can be due to the mucociliary clearance. Nevertheless, signals obtained from the stomach were way lower than signals obtained from the lungs.

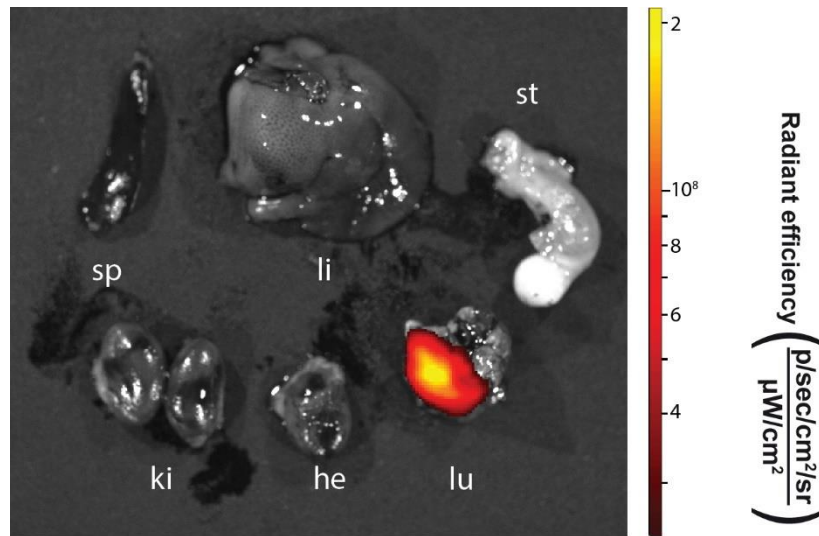


**Figure 17: 24h 2D epifluorescence imaging of organs ex vivo after intratracheal pulmonary delivery of quantumdots.** After treating female BALB/cRj mice with quantumdots (containing 10 $\mu$ g AF750- siRNA) via the intratracheal route animals were sacrificed after 24h and their organs imaged ex vivo. A strong signal was obtained in the lungs whilst no signals were observed in other organs. Sp: spleen; li: liver; st: stomach; ki: kidneys; he: heart; lu: lungs. (n=3, representative animal is shown)

Due to the strong signal in the lungs 0h and 24h after application and the absence of further significant signals in other organs (despite the low stomach signal) it can be concluded that QDs remain in the lungs. There was no detectable renal excretion. This makes QDs a good choice as a vehicle for other substrates which should stay in the lungs and without passing the blood- air-barrier and as a result being excreted. Also, after optimization, such a pattern was observed in almost all animals (5/6) which were successfully treated intratracheally with QDs.

#### 4.2. Pulmonary delivery of Auropolyplexes: in vivo tracking of siRNA by NIR fluorescence imaging

The optimized protocols from intratracheal administration of QDs and NIR FLI imaging were further used to study pulmonary delivery of siRNA after intratracheal aerosolization of Auropolyplexes (gold nanoparticle formulation loaded with AF750-siRNA). 75 $\mu$ l of the Auropolyplexes were applied intratracheally in BALB/c mice using the Penn Century sprayer as described in the intratracheal instillation section (3.2). The animals tolerated this amount and showed no signs of respiratory distress. The epifluorescent imaging was performed as described in the imaging section (3.3) according to the technical notes released by PerkinElmer. For image analysis the “manual spectral unmixing process” was used. This tool distinguishes between background signal and AF750 signal (with excitations of 675 nm and 725 nm) by deducting the calculated mixed autofluorescence/AF750 signal for each pixel.

After intratracheal application of the gold nanoparticles (Auropolyplexes), the fluorescent signal was found in the thoracic area in prone and supine positioning. (Fig. 18) This indicates the successful application and equal distribution of the AuNPs in the lungs.

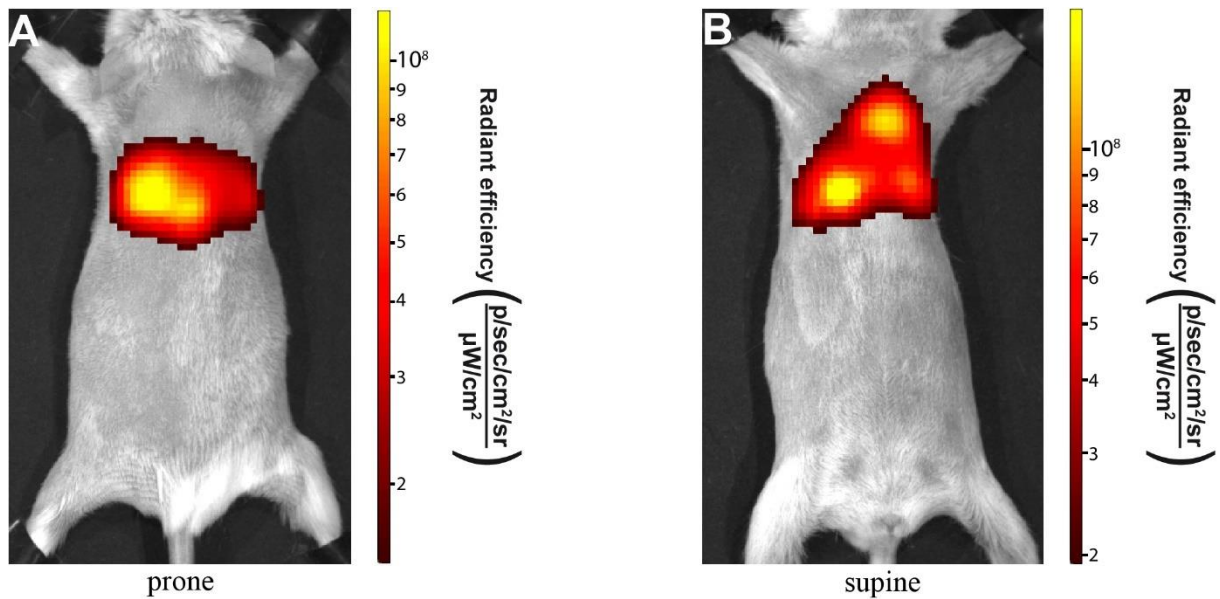


**Figure 18: 0h 2D epifluorescence imaging of Auropolyplexes after intratracheal pulmonary delivery.** Female BALB/cJRj mice were treated with ALSL 10 Auropolyplexes (containing 10 $\mu$ g AF750-siRNA) intratracheally and imaged immediately after application in prone and supine position for AF750 signal. In both positions a strong signal is observed from the thoracic area indicating a successful application in the lungs. Color coded fluorescence radiance images are overlaid onto reflected light images. (n=3, representative animals are shown.)

24h after administration the animals were imaged a second time. Hereby the signal strength in the thoracic area is lower, whereas a high signal is observed in the abdominal area. When imaged in prone position, the signal localization indicates enrichment in the kidneys. (Fig. 19 A) When imaged in supine positioning the strongest signals were observed in the bladder area. (Fig. 19 B)

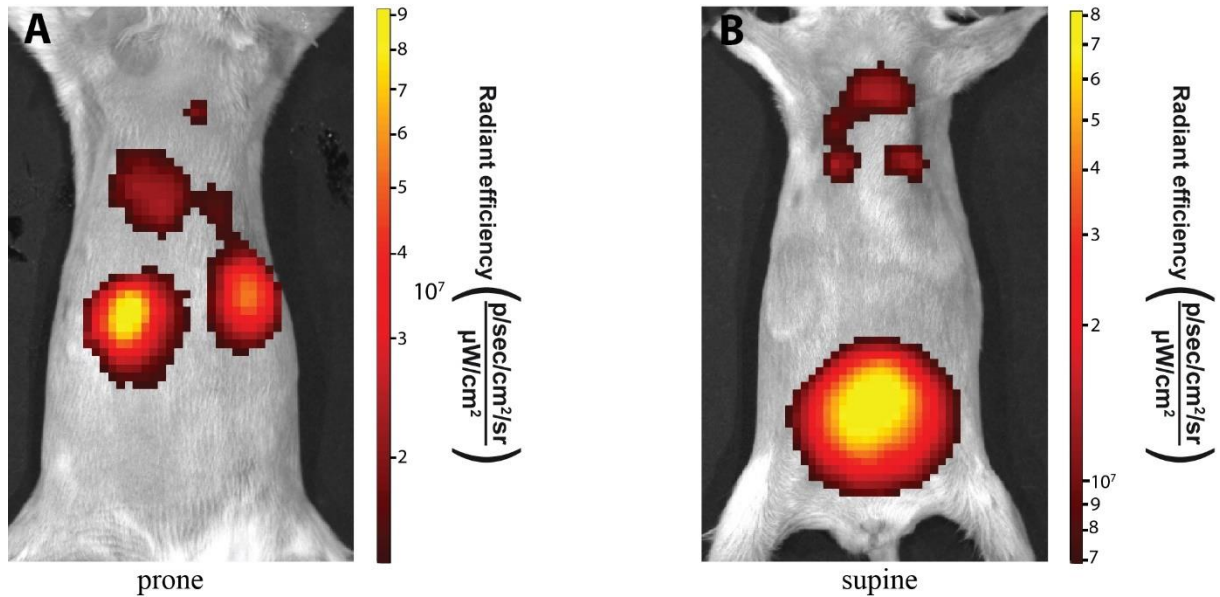


**Figure 19: 24h 2D epifluorescence imaging of Auropolyplexes after intratracheal pulmonary delivery.** Female BALB/cJRj mice were treated with ALSL 10 Auropolyplexes (containing 10 $\mu$ g AF750-siRNA) intratracheally and imaged 24h thereafter in prone and supine position. (A) In prone position strong signals are observed in the anatomical area of the kidneys. (B) In supine position strong signals are observed in the anatomical region of the bladder. In both positions slight signals remain in the thoracic area. Color coded fluorescence radiance images are overlaid onto reflected light images. (n=3, representative animals are shown.)

Signal quantification was done by placing ROIs on the thoracic and abdominal area in whole animal 2D FLI (0h and 24h). In prone as well as in supine positioning the ROI intensities of the abdominal area was increased after 24h, whereas the intensities in the thoracic region were lower or remained nearly the same, depending on the positioning of the animal. (Fig. 20, 21).

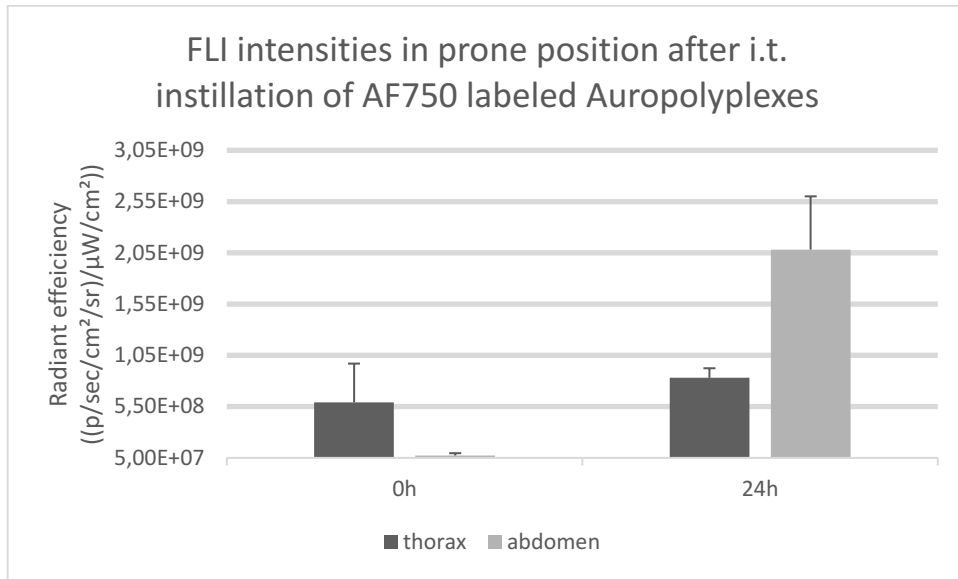


**Figure 20: FLI biodistribution of AF750-siRNA after intratracheal application in prone position.** Animals were treated with ALSL (10  $\mu\text{g}$  Alexa750-siRNA) as described. 24h after instillation a clear rise in the ROIs signals strength is observed from the abdomen. Signal strengths coming from the thoracic area nearly remain the same. (Values represent the means  $\pm$  SD of data obtained from 3 animals per group).

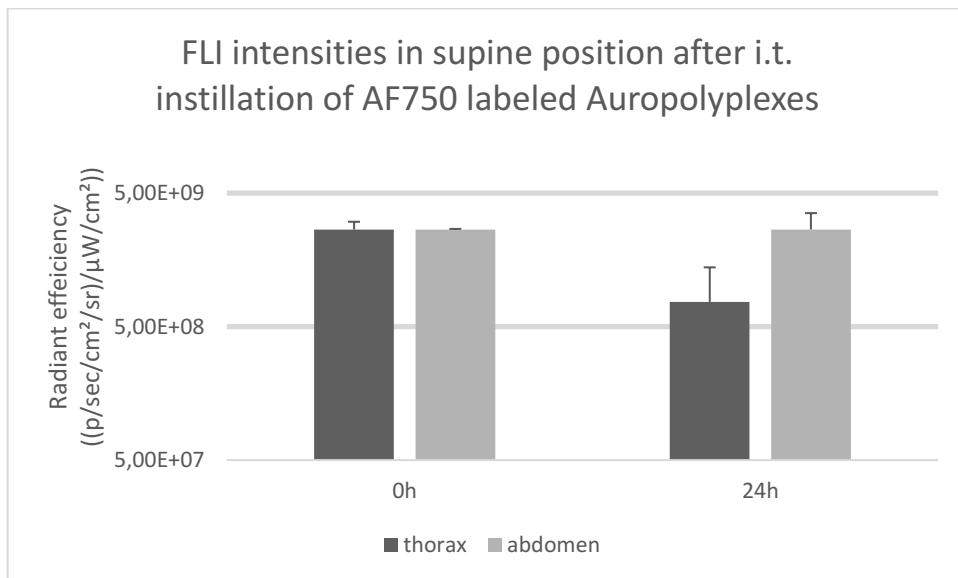


**Figure 21: FLI biodistribution of AF750-siRNA after intratracheal application in supine position.** Animals were treated with ALSL (10  $\mu\text{g}$  Alexa750-siRNA) as described. 24h after instillation the proportion of the signal strengths move to the abdominal area. Signal strengths in the thoracic area diminish. (Values represent the means  $\pm$  SD of data obtained from 3 animals per group).

To confirm the localization of the fluorescence signal of the 0h and 24h imaging time points, i.p. injection of the contrast agent Iopamidol was done to allow contrast agent enhanced CT. At the 0h imaging time point the signal could clearly be dedicated to the lungs (Fig. 22 A), at the 24h time point both to the lungs and the organs of the renal system (kidney, bladder). (Fig. 22 B)

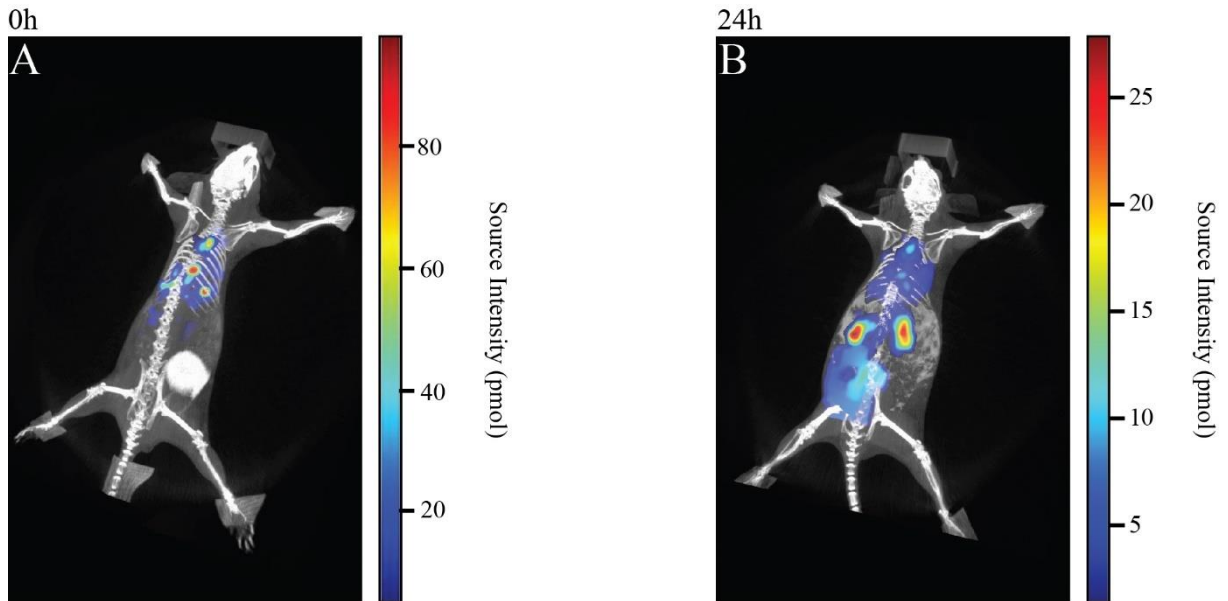


**Figure 22: FLIT/CT imaging of AF750-siRNA after intratracheal application. (A)** Imaged directly after application. A bright signal is obtained in the lungs. **(B)** 24h after application, the signal in the lungs is attenuated and a bright signal is obtained in the kidneys and the bladder. Color coded fluorescence radiance images are overlaid onto CT images. ( $n=3$ , representative animals are shown.)

After imaging the animals in 2D FLI and with FLIT/ CT the animals got sacrificed via cervical dislocation. Thereafter the organs were imaged in 2D FLI. Hereby a strong signal was obtained in the lungs and the kidneys. (Fig. 23)

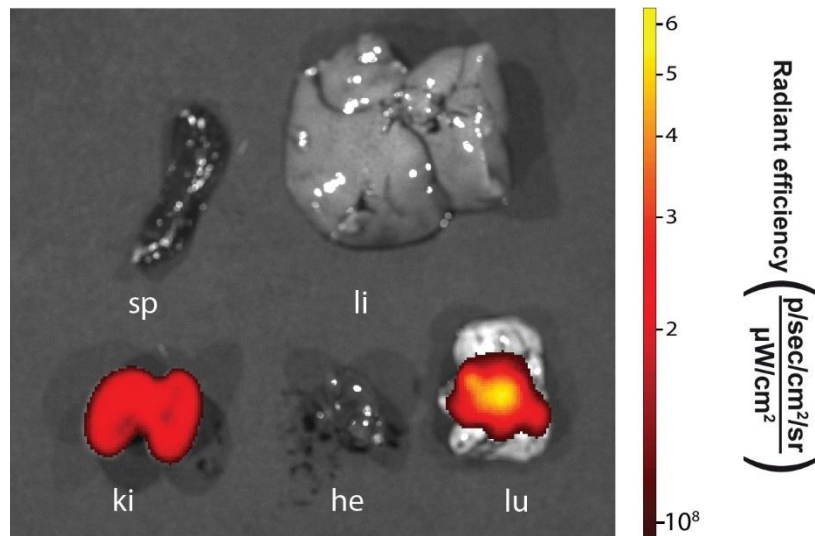


**Figure 23: 24h 2D epifluorescence imaging of organs ex vivo after intratracheal pulmonary delivery of AF750 siRNA- labelled Auropolyplexes.** When treating female BALB/cRj mice with ALSL 10 auropolyplexes (containing 10 $\mu$ g AF750- siRNA) via the intratracheal route animals got sacrificed after 24h and their organs were imaged ex vivo. A strong signal was obtained in the lungs and the kidneys. Sp: spleen; li: liver; st: stomach; ki: kidneys; he: heart; lu: lungs. (n=3, representative organs are shown)

Taken together, after 24h there is a trend towards a reduced signal in the thoracic area and an increased signal in the abdominal area. Nevertheless, direct quantification is not significant with FLI because of the strong impact of tissue absorption on the signal strength. This circumstance is clearly shown by the differences/ absences of signals in the images taken in prone and supine positioning at the same timepoint as well as the total amount of signal strength measured in different timepoints. Nevertheless, the first imaging directly after instillation shows a bright signal in the thoracic area, the lungs. Within 24h it is followed by an air- blood- transfer and then by renal excretion of most of the applied material. This is confirmed by combined CT/ FLIT measurement, where additional signals in the anatomical localization of the kidneys and the bladder occur, as well as measurements in 2D FLI of the organs *ex vivo*. Here the signal was clearly dedicated in the lungs and the kidneys. siRNA- AF750 therefore is, when applied via intratracheal instillation, excreted via the renal system within 24h.

#### 4.3. Monitoring CD49f targeted transgene gene delivery to breast cancer lung metastases by bioluminescence imaging

Gene delivery polyplexes were intratracheally administered into mice carrying CD49f overexpressing lung tumor lesions within the 4T1 murine triple negative breast cancer model and investigated for luciferase transgene expression by bioluminescence imaging. The monitoring of the tumor growth was conducted with T2 weighted MR imaging. Hereby the tumor tissue was visible as hyperintense structures. Differentiation of tumor tissue and artefacts (e.g. coming from blood vessels) was done by comparing the treated animals with an untreated control animal. At day 10 or 11 *post implantationem* a high tumor load was observed, which was assessed as sufficient for transfection studies. Firefly luciferase reporter gene loaded polyplexes were prepared by mixing plasmid DNA (encoding for firefly luciferase reporter gene) with either targeted version of LPEI (LPEI-PEG-CD49f) or non-targeted PEG control (LPEI-PEG). 75µl of the polyplex solution were applied via intratracheal instillation with the Penn Century sprayer as described in the i.t. section. The animals showed no signs of respiratory distress. 24h post treatment transfection efficiency was evaluated by 2D bioluminescence imaging. The 2D-BLI images were compared with the MRI images and a co-localization of tumor tissue and BLI signal could be observed. (appendix, [Fig. 34](#))

When treated with LPEI-PEG and LPEI-PEG-CD49f a clear signal was obtained in one or both lung sites. ([Fig. 24](#)) This indicates that transfection of cancer tissue was successfully achieved in both groups.

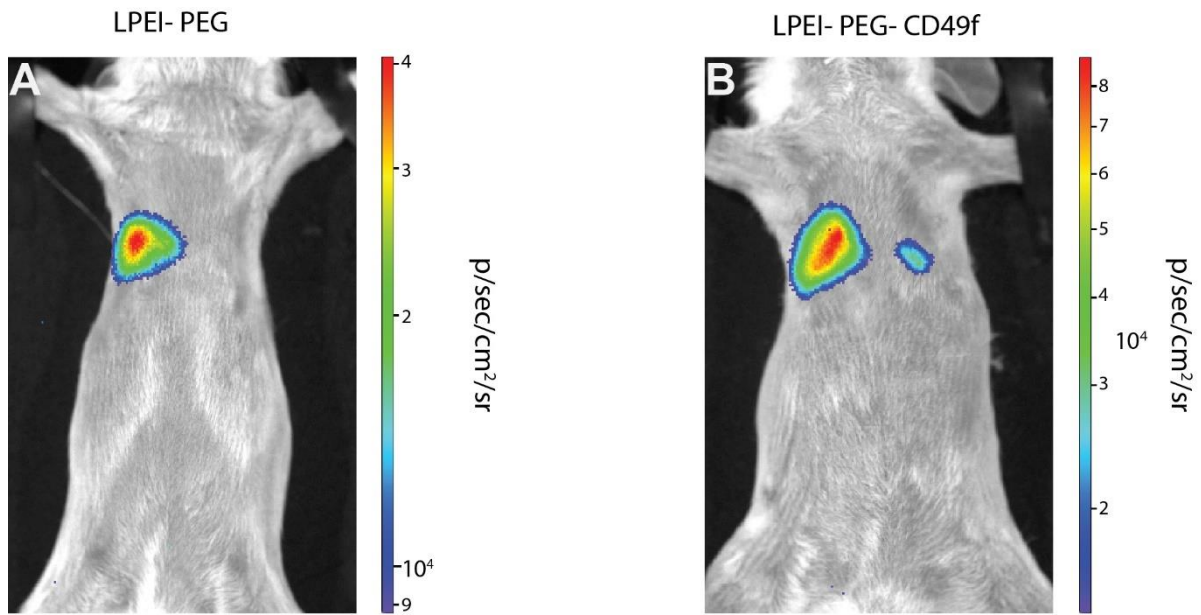


**Figure 24: 2D bioluminescence imaging after injection of LPEI-PEG and LPEI-PEG-CD49f** After injecting the 4T1-iRFP720 cancer cells *i.v.* in BALB/cJRj mice and injecting LPEI-PEG (control group (A)) or LPEI-PEG-CD49f (B) intratracheally on day 11 or 12 (depending on tumor load), animals were imaged in 2D BLI 24h thereafter. Both mice show signals in the thoracic area indicating a successful transfection of the tumor bearing lungs.  $n=3$  per group, representative animals are shown.

The BLI signal was in direct correlation with accessibility of lung tissue. In one animal the whole left lung showed hyperintense structures in MRI. (appendix, [Fig. 33](#)) This enormous tumor load led to collapse of the lung and reduced accessibility of tumor tissue through the airways resulting in decreased transfection and signal intensity in BLI.

When comparing the signal intensities of the BLI measurements the LPEI-PEG-CD49f group showed on an average 3-fold higher intensity ( $6.8 \times 10^5$ ). ([Fig. 25](#)) Considering this both groups lead to transfection but in the LPEI-PEG-CD49f group gene delivery was more efficient.

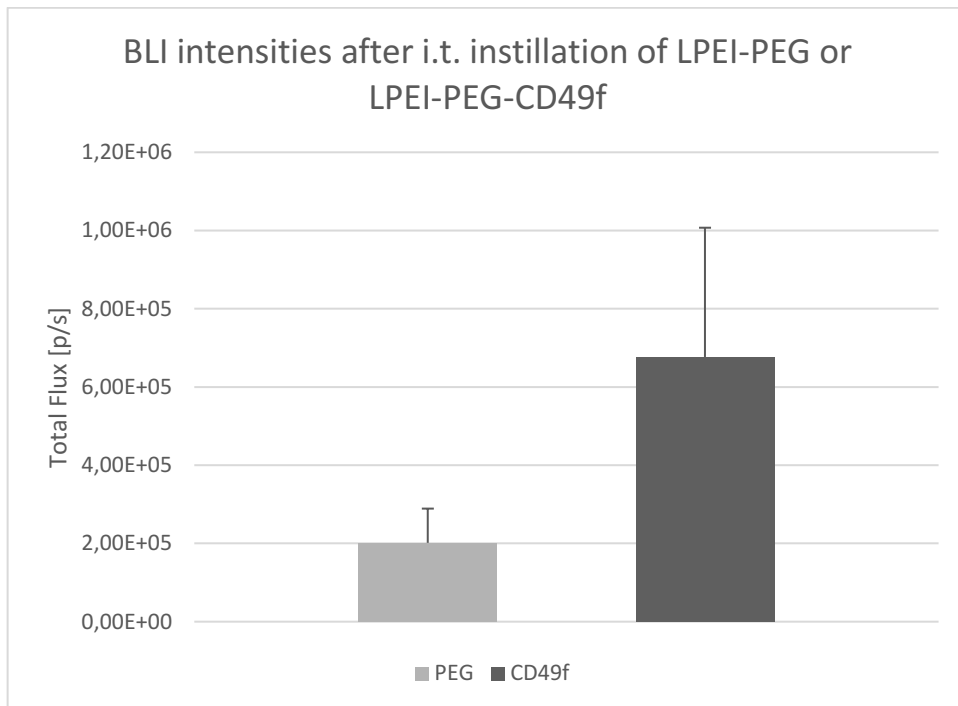


**Figure 25: BLI signal intensity comparison of LPEI- PEG and LPEI-PEG-CD49f treated animals.** After injecting the 4T1-iRFP720 cancer cells i.v. in BALB/cJRj mice and injecting LPEI-PEG (control group) or LPEI- PEG- CD49f intratracheally on day 11/12 (depending on tumor load), animals were imaged in 2D BLI 24h thereafter. A 3-fold higher ( $6.8 \times 10^5$ ) signal is obtained in animals treated with LPEI-PEG-CD49f. (Values represent the means  $\pm$  SD of data obtained from 7 animals per group).

#### 4.4. BLI within an immune-gene therapy approach by CD47 blockage and immune activation

In the last part of the thesis, the *in vivo* imaging part of an immune-gene therapy approach was conducted. Firefly luciferase expressing MDA-MB-231 cells treated with either immune-gene therapy polyplexes (loaded with IL2-P-Fc gene) or control polyplexes or untreated cells were implanted subcutaneously in SCID mice and tumor growth was followed by bioluminescence imaging. The goal was to see if the IL2-P-Fc based immune-gene therapy transfected tumor cells grew differently than the control cells *in vivo*. The proposed hypothesis is that IL2-P-Fc fusion protein blocks the interaction of CD47 (on cancer cells) with SIRP $\alpha$  (on macrophages) and therefore inhibits the “don’t eat me” signal which cancer cells employ to evade immune system. (Weiskopf et al. 2016) The IL2- part is needed for the secretion of the novel fusion protein and the Fc- part (from immunoglobulin G) leads to an additional activation of the immune system. Triple negative human breast cancer cell line MDA-MB-231 LM2-4 was stably marked with lentivirus to express a fusion protein of firefly luciferase and enhanced green fluorescent protein (EGFP<sub>luc</sub>) so that they can be tracked *in vivo* with BLI. After transfection with either IL2-P-Fc polyplexes or control plasmid,  $1 \times 10^6$  cells were injected s.c. at the location of the 4<sup>th</sup> mammary gland pair of CB17.SCID mice. To monitor the tumor growth 2D BLI was done after s.c. injection in the neck of Luciferin (30mg/kg BW) on an IVIS spectrum -CT imaging system (PerkinElmer). For quantification ROIs have been placed on the inguinal area of each animal. In BLI there is a direct correlation of signal intensity and tumor size/ amount of tumor cells. Therefore, the intensities measured with the ROIs directly represent the tumor size in each timepoint.

Eight days after injection of the tumor cells exponential tumor growth in the control group was observed. In contrast, in the bb-mCherry and more pronounced in the IL-2-P-Fc group tumor growth was reduced. ([Fig. 26](#))

The long-time study revealed that the IL2-P-Fc treated group shows no growth until imaging day 10. Up to this time point tumor size even decreased. However, after imaging at day 10 the tumor size increased until day 28. After this timepoint no further growing of the tumor was observed in this group, whilst tumor sizes in both control groups still increased. ([Fig. 27](#))

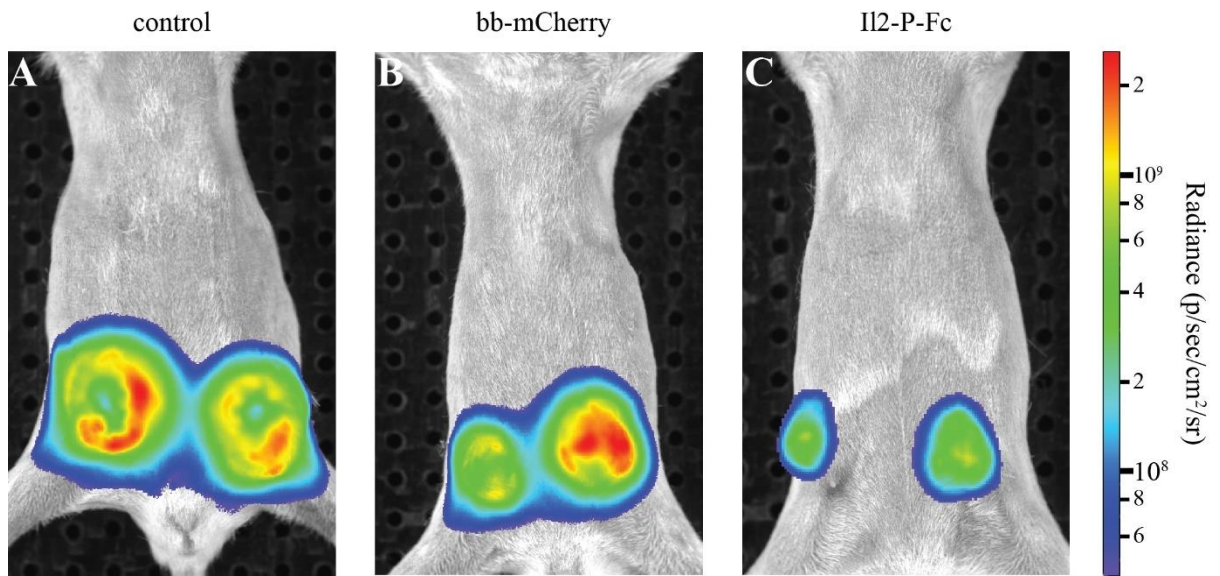


**Figure 26: 2D bioluminescence imaging 8 days after injection of  $1 \times 10^6$  MDA-MB-231 EGFP-luc human breast cancer cells.** 8 days after injection of  $1 \times 10^6$  EGFP-luc MDA-MB-231 human breast cancer cells s.c. in the region of the 4<sup>th</sup> mammary gland of female CB17.SCID mice a hindered growth in the IL2-P-Fc-group (C) is seen when compared to both control groups (A) (B). (n=3 per group, representative animals are shown.)

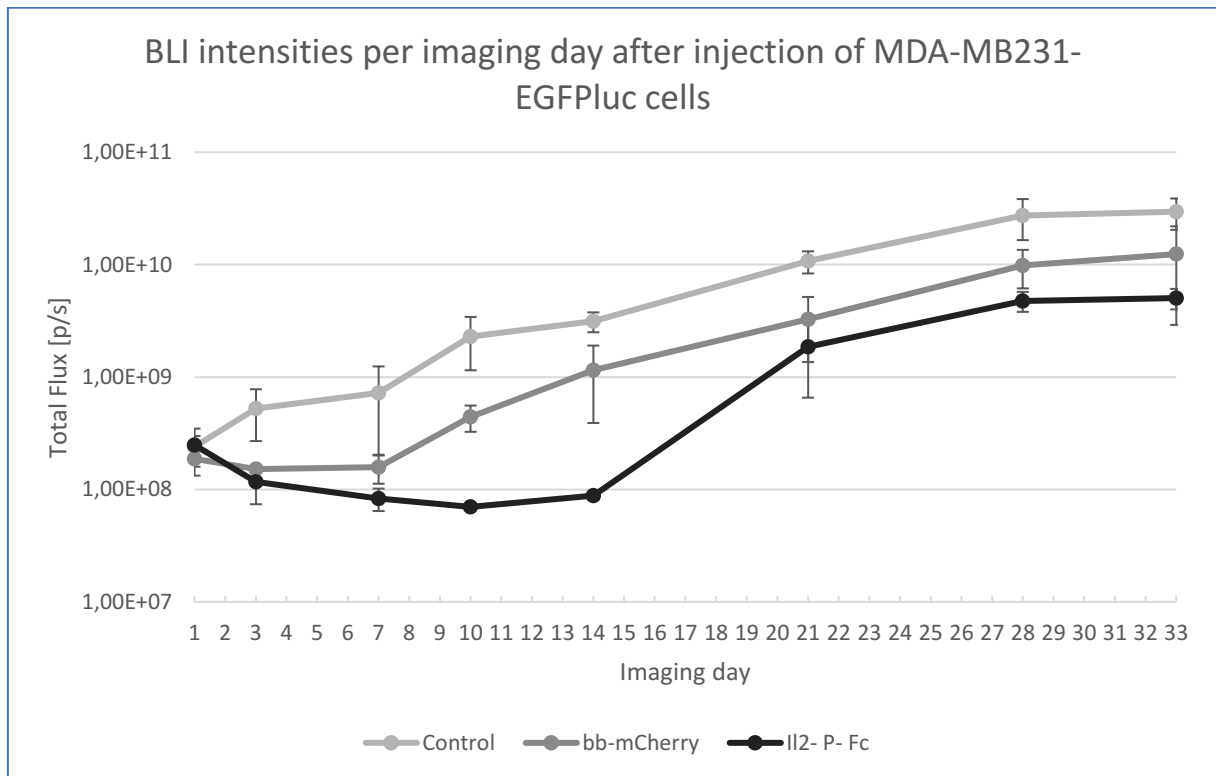


**Figure 27: Timescale of 2D bioluminescence signal strength after injection of  $1 \times 10^6$  MDA-MB-231 EGFP luc human breast cancer cells.** On imaging day 1  $1 \times 10^6$  MDA-MB-231 EGFP luc cells have been injected s.c. in the region of the 4<sup>th</sup> mammary gland of CB17.SCID mice. Signal intensities (and therefore tumor cell amounts) were measured after setting ROIs on the inguinal area. The untreated control group (**Control**) shows an unhindered, nearly exponential growth whilst growth of the stained control group (**bb-mCherry**) is hindered. The growth of the IL2-P-Fc group (**IL2-P-Fc**) shows no growth until day 10 and afterwards starts to grow very slowly. (Values represent the means  $\pm$  SD of data obtained from 3 animals per group)

The tumor cells of the untreated control group are, due to CD47, not detected by the innate immune system. This leads to their unhindered growth. The backbone stain, which was tested in the bb-mCherry group, seems to have an impact on the tumor growth or the immune response towards the tumor cells. The reason for this stays unclear.

The BLI signal of tumor cells of the IL2-P-Fc group did not increase until day 10. This can be explained by the innate immune systems response and the reduced angiogenesis. In this group the Signal regulatory protein  $\alpha$  (SIRP $\alpha$ ) and therefore the “anti-phagocytic signal “is blocked, which enables SIRP $\alpha$ - positive immune cells to recognize the tumor cells and inactivate them.

This leads, as described in the CD47 chapter ([1.4.2.2](#)), additionally to a decreased angiogenesis, which can also slow down tumor growing in this group. Ten days after transplantation the tumor cells then start to grow. The stagnation of tumor growth in all 3 groups after day 28 of imaging can be due to limitations in angiogenesis and resulting limited supply in nutrients needed for tumor growth.

## 5. Conclusion

In this diploma thesis fluorescence and bioluminescence imaging techniques in combination with CT and MRI have been used to answer questions of biodistribution, targeted gene delivery and immunogen therapy. In both biodistribution studies, FLI has been used due to its high spatial resolution and signal strength, which make a precise location of the received signals possible.

In the Quantumdot project, the biodistribution study after intratracheal instillation has been done with epifluorescence imaging at time point 0 and after 24 h post treatment. The first imaging session directly after application of the Quantumdots showed the successful delivery in the lungs. Twenty-four hours after instillation a second epifluorescence imaging session of the animal followed by imaging of the organs *ex vivo* informed about the biodistribution. Hereby it was shown that Quantumdots injected via the intratracheal route remain mostly in the lungs and are not excreted or enriched in any other organs.

In the Auropolyplex project, the biodistribution study after intratracheal instillation has been done with epifluorescence imaging and FLIT/CT. Directly after application of the Auropolyplexes the FLI showed the successful delivery in the lungs. 24h after application a second epifluorescence imaging session followed by FLIT/CT showed the biodistribution of the AF750 labelled siRNA. To confirm the results the organs have been imaged with FLI afterwards. When injecting AF750 labelled siRNA with Auropolyplexes via intratracheal instillation siRNA is excreted via the organs of the renal system within 24h.

In the targeted gene delivery project (CD49f) and the immunogen therapy project (CD47) bioluminescent imaging was used due to the correlation of signal strength and bioluminescent-labeled cells.

In the targeted gene delivery project (CD49f) and the immunogen therapy project (CD47) bioluminescent imaging was used to track gene delivery and tumor growth, respectively. In the CD49f targeted gene delivery project 4T1-iRFP 720 human breast cancer cells have been injected in the lateral tail vein. Tumor growth has been observed with MRI. After reaching an adequate tumor size for transfection LPEI-PEG or LPEI-PEG-CD49f cells have been injected via the intratracheal route. 24 h after instillation the successful delivery to the lungs as well as the successful gene delivery to the tumor bearing regions has been shown by combination of

MRI and BLI. The LPEI-PEG-CD49f group hereby leads to a more successful transfection when compared with the control group.

In the CD47 project MDA-MB-231 EGFP<sub>luc</sub> human breast cancer cells have been injected s.c. in the region of 4<sup>th</sup> mammary gland. Hereby one group received untransfected cells, one group bb-mCherry transfected cells as control and the last group IL2-P-Fc transfected cells. Tumor growth has been observed by eight BLI imaging sessions over 33 days. In the IL2-P-Fc group no tumor growth was seen until day 14. Until day 33 the growth of the injected tumors was hindered in the IL2-P-Fc and the bb-mCherry group. Whilst the hindered growth in the IL2-P-Fc group can be explained by interactions of the innate immune system the hindered growth in the bb-mCherry group remains unclear. If the hindered growth in the IL2-P-Fc is due to SIRP $\alpha$  or the Fc region will be the focus of following studies.

## 6. Appendix

## 6.1. QD FLI biodistribution data

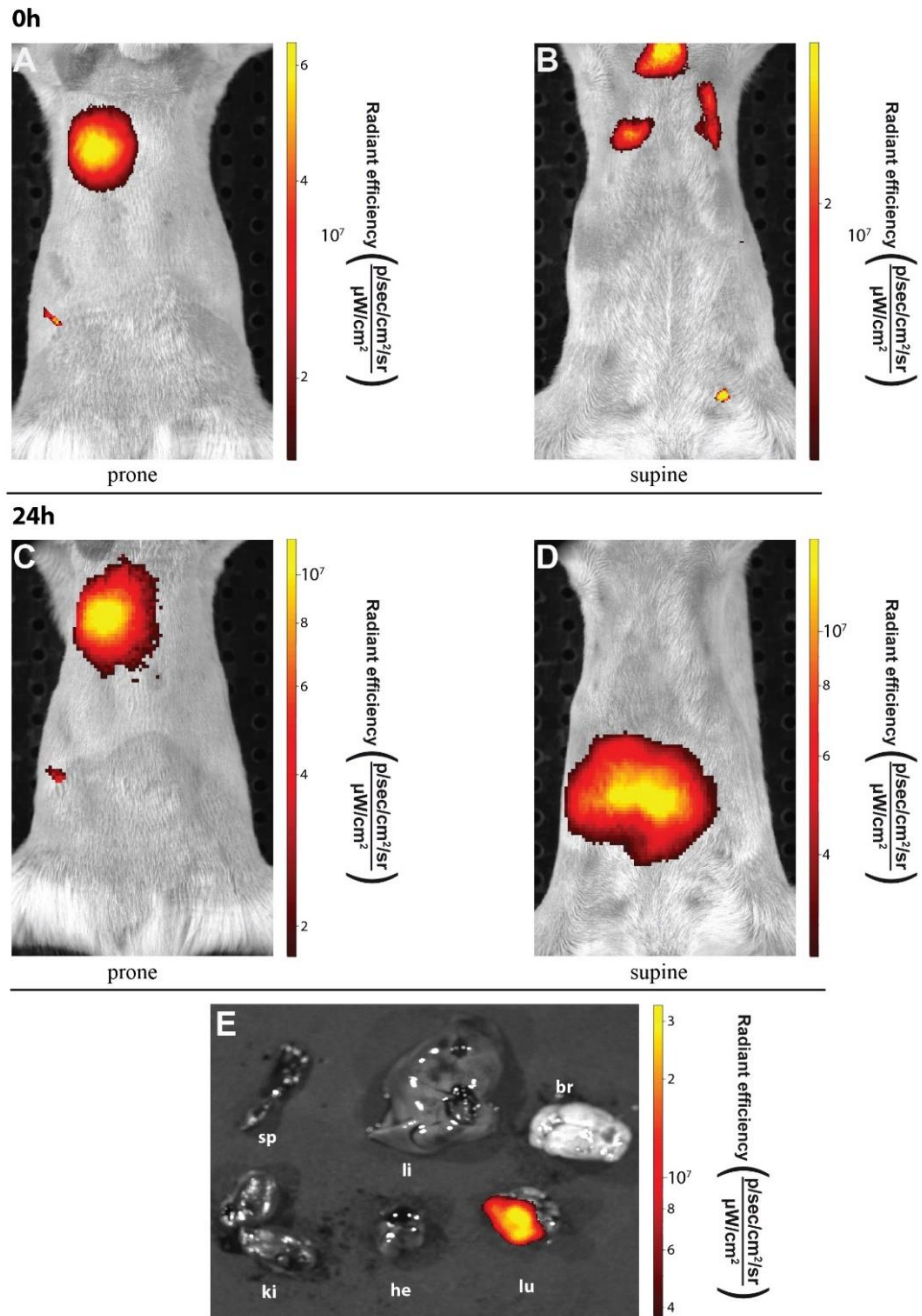


**Figure 28: Supplementary QDs data.** *In vivo* biodistribution with QDs. When imaged directly after administration (A; B) a clear signal is obtained in the lungs. 24h after application the signal remains in the lungs (C). In supine positioning a signal is obtained in the abdominal area. (D) The organs imaged *ex vivo* show a signal only in the lungs. (sp: spleen, li: liver, br: brain, ki: kidneys, he: heart, lu: lungs). There was no penetration of the blood brain barrier. The signal in the abdominal area could be due to swallowing after application.

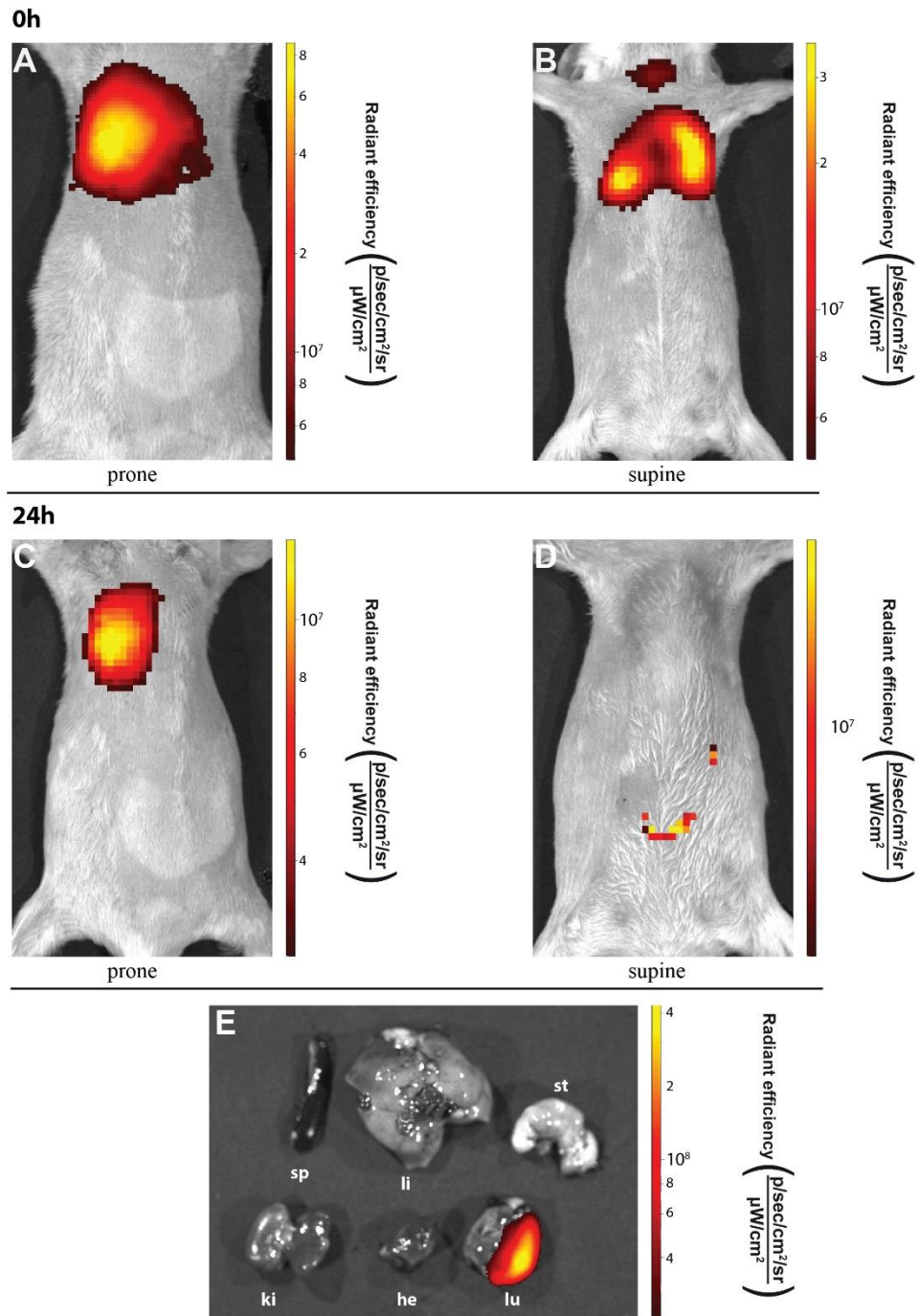


**Figure 29: Supplementary QDs data.** When imaged directly after administration (A; B) a clear signal is obtained in the lungs. In supine positioning (B) a small signal is obtained in the cranial parts of the trachea due to the application route. 24h after application the signal remains in the lungs (C). In supine positioning a very low signal is obtained in the abdominal area which can be classified as an artefact (D) The organs imaged ex vivo show a signal only in the lungs. (sp: spleen, li: liver st: stomach, ki: kidneys, he: heart, lu: lungs).

## 6.2. Auropolyplex FLI and FLIT/CT biodistribution data

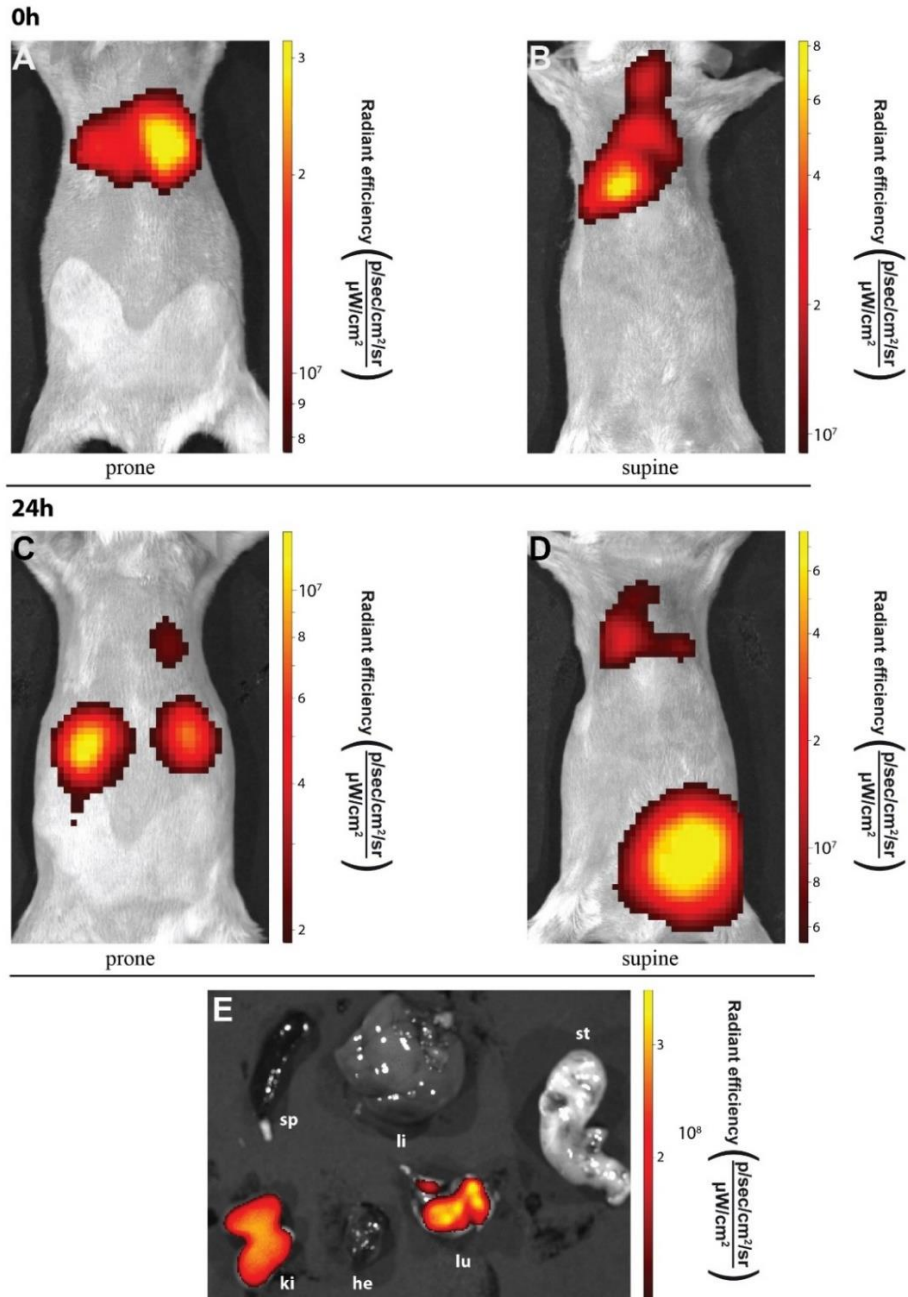


**Figure 30: Supplementary Auropolyplex data.** Directly after application a bright signal is obtained in the thoracic area indicating a successful delivery of the AuNPs in the lungs (A,B). In supine positioning a signal is also obtained in the tracheal area due to the application route (B). 24h after application in prone positioning a bright signal is seen in the anatomical localization of the kidneys (C). In supine positioning a signal is obtained from the thoracic area and the anatomical localization of the bladder (D). The organ imaging shows a bright signal in the lungs as well as the kidneys indicating a renal elimination of the AuNPs within 24h. (E) (sp: spleen; li: liver; st: stomach; ki: kidneys; he: heart; lu: lungs)

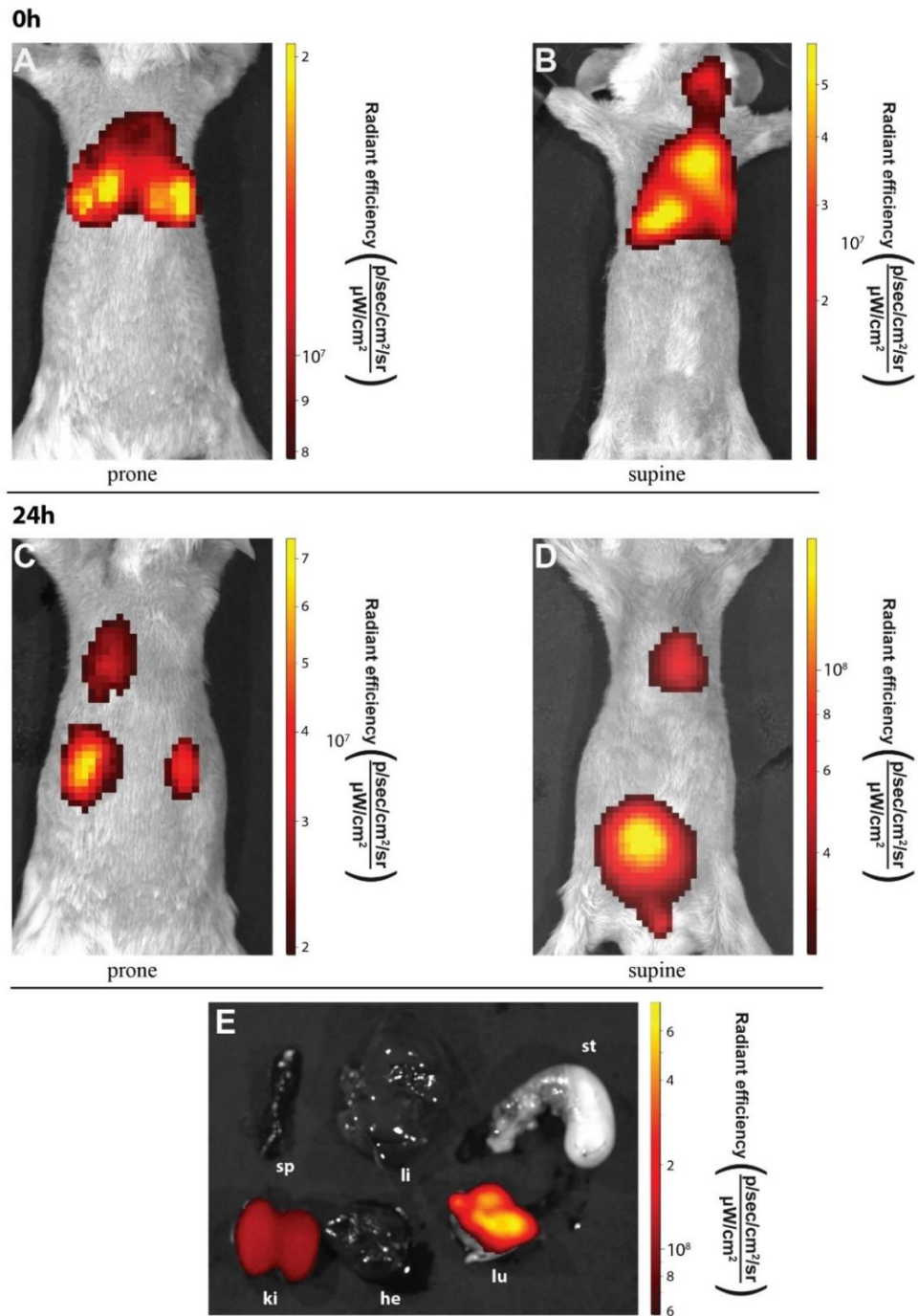


**Figure 31: Supplementary Auropolyplex data.** Directly after application a bright signal is obtained in the thoracic area indicating a successful delivery of the AuNPs in the lungs (A, B). The signal in the thoracic area in supine positioning is due to the application route. (B) 24h after application in supine positioning a slight signal is obtained in the thoracic and a bright signal in the abdominal area. (C, D). In prone positioning the signal is in the anatomical localization of the kidneys (C), in supine in the localization of the bladder (D) The organ imaging shows a bright signal in the lungs as well as the kidneys indicating a renal elimination of the AuNPs within 24h. (E) (sp: spleen; li: liver; st: stomach; ki: kidneys; he: heart; lu: lungs)

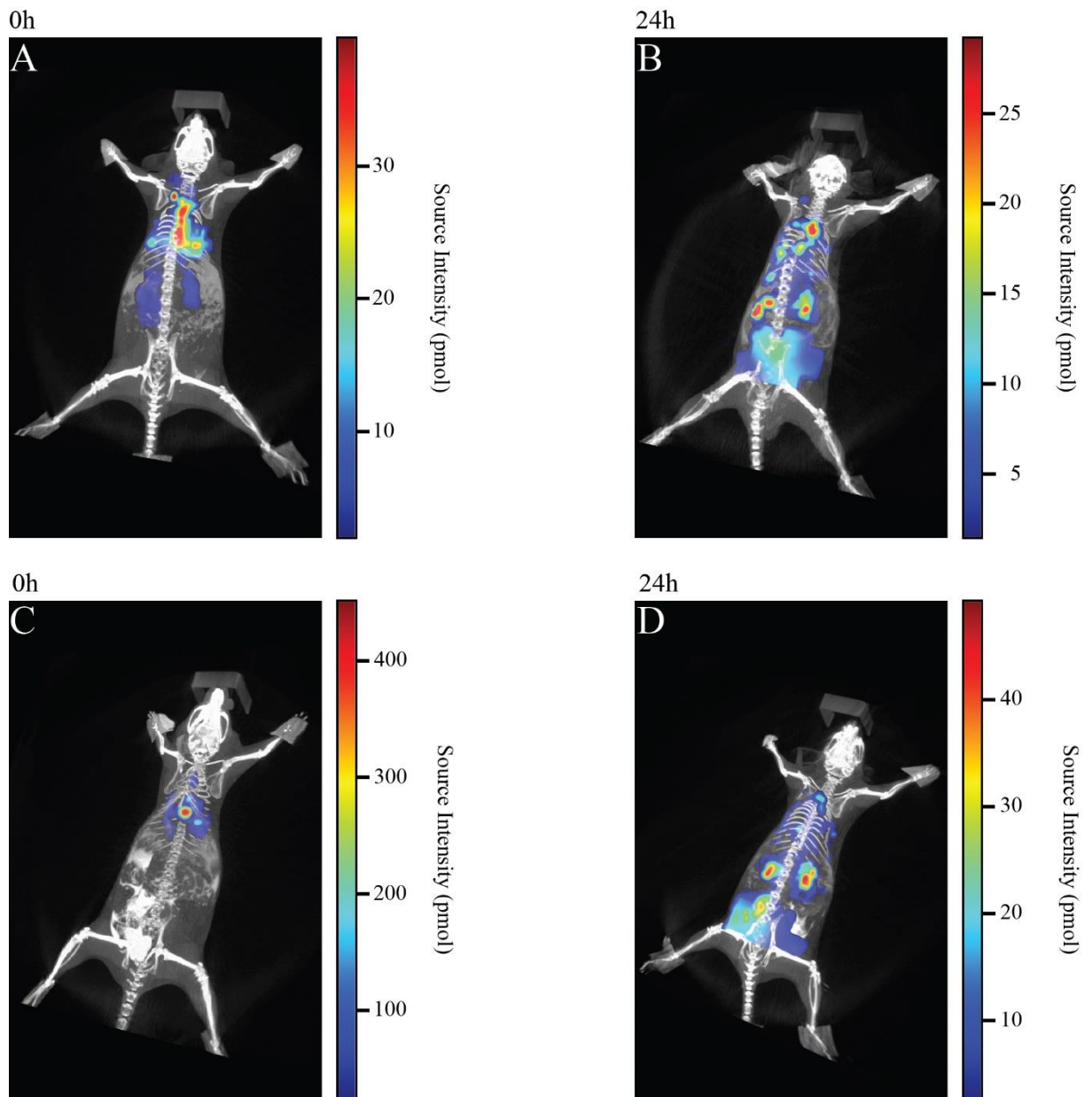


**Figure 32: Supplementary Auropolyplex FLIT/CT data.** In 0h imaging the signal can be clearly dedicated to the lungs. (A, C). In 24h imaging a signal remains in the lungs and a bright signal is also abundant in the kidneys and the bladder (B, D). This confirms the hypothesis, that the gold nanoparticles are excreted via the renal system within 24h.

### 6.3. CD49f BLI and MRI

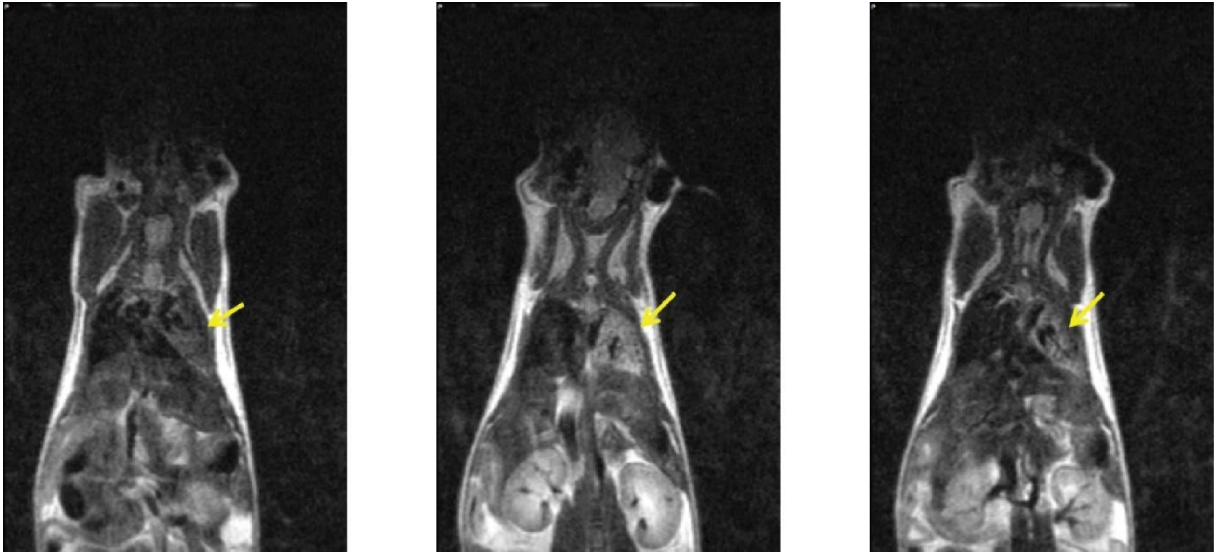


*Figure 33: Supplementary CD49f data. T2 weighted MRI of an animal with heavy tumor load. The hyperintense tumor lesions are marked with the yellow arrow. Due to the lowered ventilation of the lung transfection wasn't successful. (images by Mag. Fatih Alioglu)*

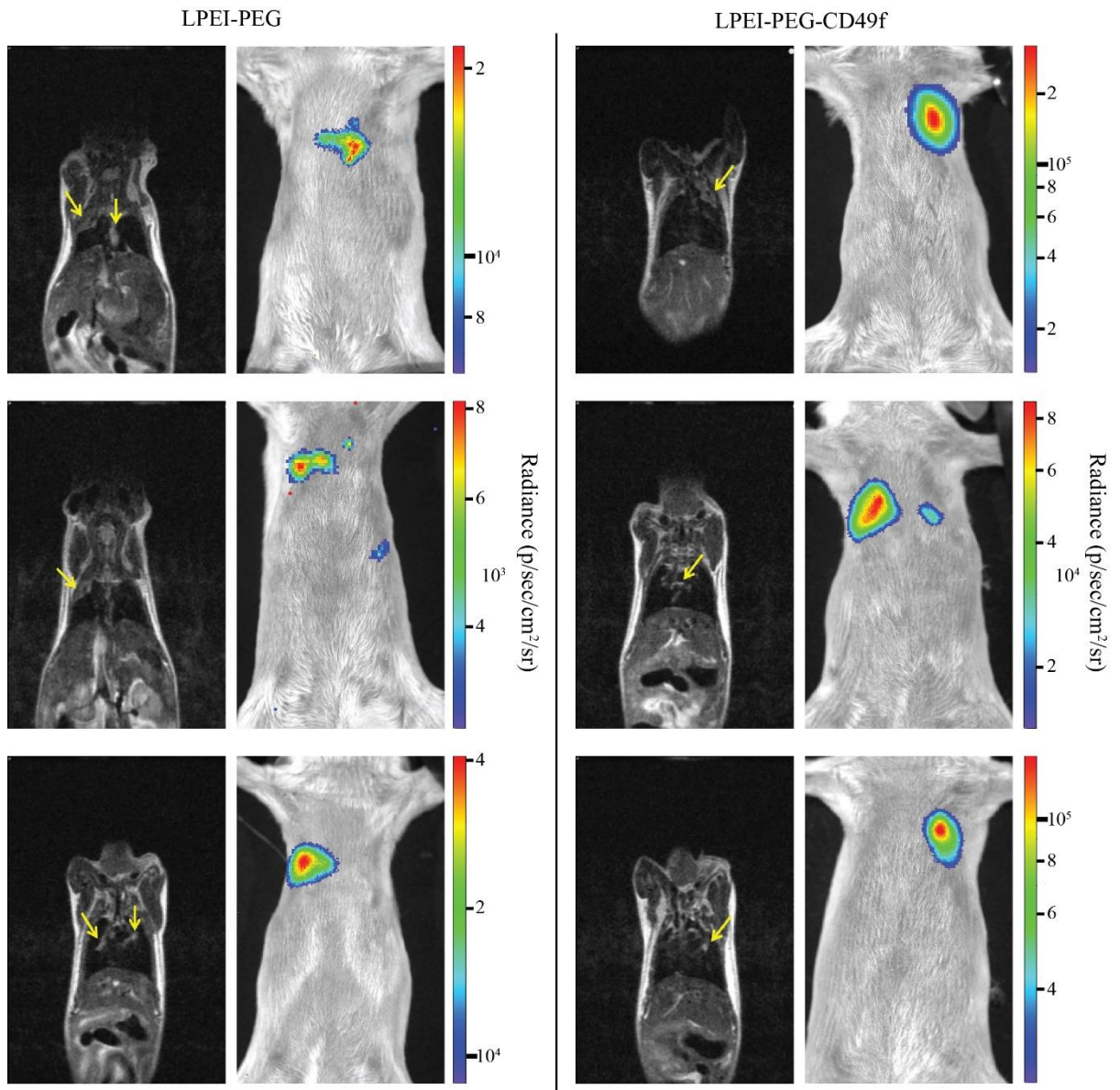


**Figure 34: Supplementary CD49f data.** Comparison of LPEI-PEG and LPEI-PEG-CD49f transfection efficiency imaged with BLI and T2 weighted MRI tumor imaging. Signals in BLI are on the same locations as tumors detected with MRI. In both groups there is successful transfection.

## 6.4. CD47 BLI

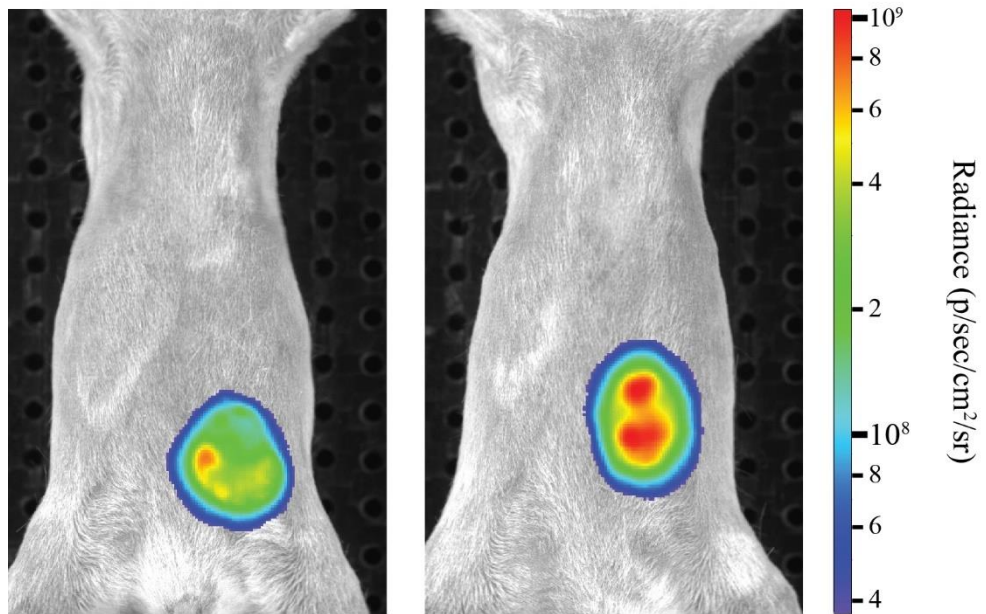


*Figure 35: Supplementary CD47 data. Animals with injected tumors in the fourth mammary complex. In both animals tumor growth was detected in just one side (left).*

## 7. Summary

Optical imaging can be divided into fluorescence imaging (FLI) and bioluminescence imaging (BLI). Whilst FLI uses fluorescent dyes, which absorb excitation light to emit light of longer wavelength, BLI is based on bioluminescence, where light is produced as a result of an enzymatic reaction within the animal. FLI can be used for spatiotemporal tracking of nucleic acid-based drugs *in vivo*. BLI, on the other hand, has way lower signal intensities but the signal strength is in direct correlation with the amount of the marked cells. Therefore, BLI can be used for tracking gene delivery or tracking exact biological processes. In both imaging modalities, background noise is a big problem. To reduce background coming from the food in the gastrointestinal tract it is necessary to set the animals on a low fluorescent diet prior to experiments. Besides this, shaving the animals can increase the signal intensities significantly.

When applying drugs or nucleic acids in the lungs, local administration from the airway side has many benefits when compared to systemically administration. This thesis includes fluorescent imaging to track nucleic acid-based drugs *in vivo* for studying biodistribution and bioluminescence imaging for investigating gene delivery in tumor models or longitudinal tracking of tumor growth. The FLI biodistribution studies, one using intratracheally applied quantumdots (QDs) and the other using gold nanoparticles (Auopolyplexes/ AuNPs) as carriers, show the big benefit of the increased signal strength for these kinds of studies. Whilst the Quantumdot's signal remains in the thoracic area even 24h after application, the signal in the AuNP project is redistributed to the abdominal area. Here it is shown that the applied material is excreted via the renal system within 24h. In the CD49f- project, tumor growth is monitored with both, FLI and MRI. When the LPEI- PEG/ LPEI-PEG-CD49f based polyplexes are administered intratracheally into tumor bearing mice, BLI was used to determine *in vivo* transfection of tumor area, which was visualized by MRI. In both groups transfection took place, but LPEI-PEG-CD49f group showed a 3-fold higher transfection efficiency. In the CD47- project the effects of SIRP $\alpha$ - Fc-blockade on the tumor growth is shown. Hereby the tumor cells are tagged with luciferase reporter gene and clearly show the hampered tumor growth as an effect of the blockade in the CD47-group when compared with the control groups.

## 8. Zusammenfassung

Mittels optischer Bildgebung kann sowohl die Bioverteilung von makromolekularen Substanzen als auch die Expression von Reportergenen *in vivo* verfolgt werden. Bei der Fluoreszenzbildgebung (FLI) werden Fluoreszenzfarbstoffe, die im Nahe Infrarot fluoreszieren, eingesetzt. Biolumineszenzbildgebung (BLI) basiert auf der Verwendung von Luciferasen als Reportergene, deren enzymatische Aktivität bei der Umsetzung des Substrats Photonen freisetzt. Diese werden mit einer hochempfindlichen Kamera detektiert. In dieser Arbeit wurde die lokale Applikation von Nukleinsäuren und Nanopartikeln in die Lunge durch intratracheale Aerosolisierung umgesetzt. In FLI-Bioverteilungsstudien konnten sowohl nanoskalige, fluoreszierende Quantumdots (QDs) als auch fluoreszenzmarkierte Nukleinsäuren (siRNA), für die Goldnanopartikel (Auropolyplexe / AuNPs) als Träger verwenden wurden, mit hoher Signalstärke detektiert werden. Während das Quantumdot Signal auch 24 Stunden nach der Anwendung im Brustbereich verblieb, wurde das Signal der siRNA im AuNP-Projekt auf den Abdominalbereich umverteilt. Hier konnte gezeigt werden, dass das applizierte Material innerhalb von 24h über das Nierensystem ausgeschieden wurde. In einem Gentransferprojekt mit CD49f-zielgerichteten Gentransferpartikeln wurde das Tumorwachstum von CD49f positiven Lungenmetastasen von murinem Brustkrebs sowohl mit FLI als auch mit MRI verfolgt. Die Transfektionseffizienz wurde mit BLI verfolgt und das Signal mit morphologischer Bildgebung (Magnetresonanztomografie, MRT) korreliert. Gentransferpartikel (Polyplexe) auf LPEI-PEG oder LPEI-PEG-CD49f Basis mit Plasmid kodierend für Luziferase wurden intratracheal in tumortragende Mäuse verabreicht. In beiden Gruppen fand eine Transfektion der Tumore statt, die LPEI-PEG-CD49f-Gruppe zeigte jedoch eine dreifach höhere Transfektionseffizienz. Im einem Immun-Gentherapie Projekt wurden die Auswirkungen der Blockade von CD47 and Tumorzellen durch das Fusionsprotein SIRP $\alpha$ -Fc auf das Tumorwachstum gezeigt. Hierbei wurden die Tumorzellen mit dem Luciferase-Reportergen markiert und das Tumorwachstum mittels BLI verfolgt. Deutlich gehemmtes Tumorwachstum als Folge der Blockade in der CD47-Gruppe konnte im Vergleich zu den Kontrollgruppen gezeigt werden.

## List of abbreviations

AF750	-	AlexaFluor 750
AuNP	-	Gold nanoparticles/ Auropolypexes
BLI	-	Bioluminescent imaging
BPEI	-	branched polyethyleneimine
CCD	-	charge- coupled device
CD47	-	Cluster of differentiation 47
CD49f	-	Cluster of differentiation 49f
CSC	-	cancer stem cell
CT	-	computed tomography
FLI	-	Fluorescent imaging
FLIT	-	Fluorescent imaging tomography
FLuc	-	firefly luciferase
IgG	-	Immunoglobulin G
IVIS	-	in vivo imaging device (PerkinElmer)
LPEI	-	linear polyethyleneimine
MRI	-	Magnetic resonance imaging
NIR	-	near infrared
PEG	-	polyethylene glycol
PEI	-	polyethyleneimine
PET	-	positron emission tomography
SPF	-	severe pathogen free
QD	-	Quantumdots

QE	-	quantum efficiency
RLuc	-	renilla luciferase
ROI	-	region of interest
SCID	-	severe combined immunodeficiency
SIRP $\alpha$	-	signal regulatory protein alpha

## References

- Andersson-Engels S, af Klinteberg C, Svanberg K, Svanberg S. 1997. <http://iopscience.iop.org/0031-9155/42/5/006> (accessed May 6, 2019), 11.
- Badr CE, Tannous BA. 2011. Bioluminescence imaging: progress and applications. *Trends in biotechnology*, 29 (12): 624–633. DOI 10.1016/j.tibtech.2011.06.010.
- Ballou B, Ernst L, Waggoner A. 2005. Fluorescence Imaging of Tumors In Vivo. *Current Medicinal Chemistry*, 12 (7): 795–805. DOI 10.2174/0929867053507324.
- Bera D, Qian L, Tseng T-K, Holloway PH. 2010. Quantum Dots and Their Multimodal Applications: A Review. *Materials*, 3 (4): 2260–2345. DOI 10.3390/ma3042260.
- Bivas-Benita M, Zwier R, Junginger HE, Borchard G. 2005. Non-invasive pulmonary aerosol delivery in mice by the endotracheal route. *European journal of pharmaceutics and biopharmaceutics : official journal of Arbeitsgemeinschaft fur Pharmazeutische Verfahrenstechnik e.V*, 61 (3): 214–218. DOI 10.1016/j.ejpb.2005.04.009.
- Busato A, Fumene Feruglio P, Parnigotto PP, Marzola P, Sbarbati A. 2016. In vivo imaging techniques: a new era for histochemical analysis. *European journal of histochemistry : EJH*, 60 (4): 2725. DOI 10.4081/ejh.2016.2725.
- Caliper Life Sciences. 2007. IVIS Spectrum. Users Manual, 72.
- Castan L, José da Silva C, Ferreira Molina E, Alves Dos Santos R. 2018. Comparative study of cytotoxicity and genotoxicity of commercial Jeffamines® and polyethylenimine in CHO-K1 cells. *Journal of biomedical materials research. Part B, Applied biomaterials*, 106 (2): 742–750. DOI 10.1002/jbm.b.33882.
- Chandran PR, Thomas RT. 2015. Gold Nanoparticles in Cancer Drug Delivery. In: . *Nanotechnology Applications for Tissue Engineering*. : Elsevier, 221–237.
- Chen T, Ren L, Liu X, Zhou M, Li L, Xu J, Zhu X. 2018. DNA Nanotechnology for Cancer Diagnosis and Therapy. *International journal of molecular sciences*, 19 (6). DOI 10.3390/ijms19061671.
- Chul-Kyu P, Hoonsung C. Improvement in Tracing Quantum Dot-Conjugated Nanospheres for In Vivo Imaging by Eliminating Food Autofluorescence. *Journal of Nanomaterials*, 2015. DOI 10.1155/2015/894353.
2013. <https://www.nibib.nih.gov/science-education/science-topics/computed-tomography-ct#1021> (accessed Dec 5, 2018).
- Condeelis J, Weissleder R. 2010. In vivo imaging in cancer. *Cold Spring Harbor perspectives in biology*, 2 (12): 003848. DOI 10.1101/cshperspect.a003848.
- Driscoll KE. 2000. Intratracheal Instillation as an Exposure Technique for the Evaluation of Respiratory Tract Toxicity: Uses and Limitations. *Toxicological Sciences*, 55 (1): 24–35. DOI 10.1093/toxsci/55.1.24.

- Feldmann DP, Merkel OM. 2015. The advantages of pulmonary delivery of therapeutic siRNA. *Therapeutic delivery*, 6 (4): 407–409. DOI 10.4155/tde.15.8.
- Frangioni JV. 2003. In vivo near-infrared fluorescence imaging. *Current opinion in chemical biology*, 7 (5): 626–634. DOI 10.1016/j.cbpa.2003.08.007.
- Geyer A, Lorenzer C, Gehrig S, Simlinger M, Winkler J, Sami H, Ogris M. 2017. Fluorescence- and computed tomography for assessing the biodistribution of siRNA after intratracheal application in mice. *International journal of pharmaceutics*, 525 (2): 359–366. DOI 10.1016/j.ijpharm.2017.02.025.
- Geyer A, Taschauer A, Alioglu F, Anton M, Maier J, Drothler E, Simlinger M, Yavuz S, Sami H, Ogris M. 2017. Multimodal Fluorescence and Bioluminescence Imaging Reveals Transfection Potential of Intratracheally Administered Polyplexes for Breast Cancer Lung Metastases. *Human gene therapy*, 28 (12): 1202–1213. DOI 10.1089/hum.2017.137.
- Grooneberg DA, WITT C, WAGNER U, CHUNG KF, FISCHER A. 2003. Fundamentals of pulmonary drug delivery. *Respiratory Medicine*, 97 (4): 382–387. DOI 10.1053/rmed.2002.1457.
- Höbel S, Aigner A. 2013. Polyethylenimines for siRNA and miRNA delivery in vivo. *WIREs Nanomed Nanobiotechnology*, 5 (5): 484–501. DOI 10.1002/wnan.1228.
- Inoue Y, Kiryu S, Izawa K, Watanabe M, Tojo A, Ohtomo K. 2009. Comparison of subcutaneous and intraperitoneal injection of D-luciferin for in vivo bioluminescence imaging. *European journal of nuclear medicine and molecular imaging*, 36 (5): 771–779. DOI 10.1007/s00259-008-1022-8.
- Kalender WA. 2006. X-ray computed tomography. *Physics in medicine and biology*, 51 (13): R29-43. DOI 10.1088/0031-9155/51/13/R03.
- Keyaerts M, Caveliers V, Lahoutte T. 2014. Bioluminescence Imaging. In: . *Comprehensive Biomedical Physics*. : Elsevier, 245–256.
- Kichler A. 2004. Gene transfer with modified polyethylenimines. *The journal of gene medicine*, 6 Suppl 1: S3-10. DOI 10.1002/jgm.507.
- Krebsbach PH, Villa-Diaz LG. 2017. The Role of Integrin  $\alpha 6$  (CD49f) in Stem Cells: More than a Conserved Biomarker. *Stem cells and development*, 26 (15): 1090–1099. DOI 10.1089/scd.2016.0319.
- Kuzmov A, Minko T. 2015. Nanotechnology approaches for inhalation treatment of lung diseases. *Journal of controlled release : official journal of the Controlled Release Society*, 219: 500–518. DOI 10.1016/j.jconrel.2015.07.024.
- Leal J, Smyth HDC, Ghosh D. 2017. Physicochemical properties of mucus and their impact on transmucosal drug delivery. *International journal of pharmaceutics*, 532 (1): 555–572. DOI 10.1016/j.ijpharm.2017.09.018.
- Leblond F, Davis SC, Valdés PA, Pogue BW. 2010a. Pre-clinical whole-body fluorescence imaging: Review of instruments, methods and applications. *Journal of photochemistry and photobiology. B, Biology*, 98 (1): 77–94. DOI 10.1016/j.jphotobiol.2009.11.007.

- Leblond F, Davis SC, Valdés PA, Pogue BW. 2010b. Pre-clinical whole-body fluorescence imaging: Review of instruments, methods and applications. *Journal of photochemistry and photobiology. B, Biology*, 98 (1): 77–94. DOI 10.1016/j.jphotobiol.2009.11.007.
- Liu M, Zhang J, Shan W, Huang Y. 2015. Developments of mucus penetrating nanoparticles. *Asian Journal of Pharmaceutical Sciences*, 10 (4): 275–282. DOI 10.1016/j.ajps.2014.12.007.
- Liu Y, Cao X. 2016. Immunosuppressive cells in tumor immune escape and metastasis. *Journal of molecular medicine (Berlin, Germany)*, 94 (5): 509–522. DOI 10.1007/s00109-015-1376-x.
- Lusic H, Grinstaff MW. 2013. X-ray-computed tomography contrast agents. *Chemical reviews*, 113 (3): 1641–1666. DOI 10.1021/cr200358s.
- Mansur HS. 2010. Quantum dots and nanocomposites. *Wiley interdisciplinary reviews. Nanomedicine and nanobiotechnology*, 2 (2): 113–129. DOI 10.1002/wnan.78.
- Massoud TF, Gambhir SS. 2003. molecular imaging in living subjects: seeing fundamental biological processes in a new light. *Genes and Development*, 2003 (17): 545–580. DOI 10.1101/gad.1047403 (accessed May 6, 2019).
- Mercurio AM, Rabinovitz I, Shaw LM. 2001. The  $\alpha 6 \beta 4$  integrin and epithelial cell migration. *Current Opinion in Cell Biology*, 13 (5): 541–545. DOI 10.1016/S0955-0674(00)00249-0.
- Mir M, Ishtiaq S, Rabia S, Khatoon M, Zeb A, Khan GM, Ur Rehman A, Ud Din F. 2017. Nanotechnology: from In Vivo Imaging System to Controlled Drug Delivery. *Nanoscale research letters*, 12 (1): 500. DOI 10.1186/s11671-017-2249-8.
- Munoz R, Man S, Shaked Y, Lee CR, Wong J, Francia G, Kerbel RS. 2006. Highly efficacious nontoxic preclinical treatment for advanced metastatic breast cancer using combination oral UFT-cyclophosphamide metronomic chemotherapy. *Cancer research*, 66 (7): 3386–3391. DOI 10.1158/0008-5472.CAN-05-4411.
- Murata Y, Saito Y, Kotani T, Matozaki T. 2018. CD47-signal regulatory protein  $\alpha$  signaling system and its application to cancer immunotherapy. *Cancer science*, 109 (8): 2349–2357. DOI 10.1111/cas.13663.
- Noguchi T, Golden S. 2017. [https://www.researchgate.net/publication/315510591\\_Bioluminescent\\_and\\_fluorescent\\_reporters\\_in\\_circadian\\_rhythm\\_studies](https://www.researchgate.net/publication/315510591_Bioluminescent_and_fluorescent_reporters_in_circadian_rhythm_studies) (accessed Dec 6, 2018).
- Ntziachristos V. FLUORESCENCE MOLECULAR IMAGING.
- Patil JS, Sarasija S. 2012. Pulmonary drug delivery strategies: A concise, systematic review. *Lung India : official organ of Indian Chest Society*, 29 (1): 44–49. DOI 10.4103/0970-2113.92361.
- PerkinElmer. 2012. IVIs Spectrum CT. Hardware Manual, 86.
- Rabinovich BA, Ye Y, Etto T, Chen JQ, Levitsky HI, Overwijk WW, Cooper LJN, Gelovani J, Hwu P. 2008. Visualizing fewer than 10 mouse T cells with an enhanced firefly luciferase in immunocompetent

mouse models of cancer. *Proceedings of the National Academy of Sciences of the United States of America*, 105 (38): 14342–14346. DOI 10.1073/pnas.0804105105.

Rao J, Dragulescu-Andrasi A, Yao H. 2007. Fluorescence imaging in vivo: recent advances. *Current opinion in biotechnology*, 18 (1): 17–25. DOI 10.1016/j.copbio.2007.01.003.

Resch-Genger U, Grabolle M, Cavaliere-Jaricot S, Nitschke R, Nann T. 2008. Quantum dots versus organic dyes as fluorescent labels. *Nature methods*, 5 (9): 763–775. DOI 10.1038/nmeth.1248.

Rödl W, Schaffert D, Wagner E, Ogris M. 2013. Synthesis of polyethylenimine-based nanocarriers for systemic tumor targeting of nucleic acids. *Methods in molecular biology (Clifton, N.J.)*, 948: 105–120. DOI 10.1007/978-1-62703-140-0\_8.

Rosi NL, Giljohann DA, Thaxton CS, Lytton-Jean AKR, Han MS, Mirkin CA. 2006. Oligonucleotide-modified gold nanoparticles for intracellular gene regulation. *Science (New York, N.Y.)*, 312 (5776): 1027–1030. DOI 10.1126/science.1125559.

Sadikot RT, Blackwell TS. 2005. Bioluminescence imaging. *Proceedings of the American Thoracic Society*, 2 (6): 537-40, 511-2. DOI 10.1513/pats.200507-067DS.

Sato A, Klaunberg B, Tolwani R. 2004. In Vivo Bioluminescence Imaging. *Comparative medicine*, 54 (6): 631–634.

Shcherbakova DM, Verkhusha VV. 2013. Near-infrared fluorescent proteins for multicolor in vivo imaging. *Nature methods*, 10 (8): 751–754. DOI 10.1038/nmeth.2521.

Sherbet GV. 2017. *Molecular approach to cancer management*. London: Elsevier/Academic Press, xxi, 329 pages.

Smith BR, Gambhir SS. 2017. Nanomaterials for In Vivo Imaging. *Chemical reviews*, 117 (3): 901–986. DOI 10.1021/acs.chemrev.6b00073.

Stanford Medicine. 2018. <https://med.stanford.edu/stemcell/CD47.html> (accessed Oct 30, 2018).

Takahashi S. 2018. Molecular functions of SIRP $\alpha$  and its role in cancer. *Biomedical reports*, 9 (1): 3–7. DOI 10.3892/br.2018.1102.

Tan L, Wan A, Li H. 2014. Synthesis of near-infrared quantum dots in cultured cancer cells. *ACS applied materials & interfaces*, 6 (1): 18–23. DOI 10.1021/am404534v.

Taschauer A, Polzer W, Pöschl S, Metz S, Tepe N, Decker S, Cyran N, Maier J, Hofmann T, Ogris M, Sami H. 2019. Auopolyplex: a versatile nanotherapeutic platform for efficient nucleic acid delivery in vitro and in vivo. under revision.

Wang Y-Y, Lai SK, Suk JS, Pace A, Cone R, Hanes J. 2008. Addressing the PEG Mucoadhesivity Paradox to Engineer Nanoparticles that “Slip” through the Human Mucus Barrier. *Angewandte Chemie*, 120 (50): 9872–9875. DOI 10.1002/ange.200803526.

Weiskopf K, Jahchan NS, Schnorr PJ, Cristea S, Ring AM, Maute RL, Volkmer AK, Volkmer J-P, Liu J, Lim JS, Yang D, Seitz G, Nguyen T, Di Wu, Jude K, Guerston H, Barkal A, Trapani F, George J, Poirier JT, Gardner EE, Miles LA, Stanchina E de, Lofgren SM, Vogel H, Winslow MM, Dive C, Thomas RK, Rudin

- CM, van de Rijn M, Majeti R, Garcia KC, Weissman IL, Sage J. 2016. CD47-blocking immunotherapies stimulate macrophage-mediated destruction of small-cell lung cancer. *The Journal of clinical investigation*, 126 (7): 2610–2620. DOI 10.1172/JCI81603.
- Weissleder R. 2001. A clearer vision for in vivo imaging. *Nature biotechnology*, 19 (4): 316–317. DOI 10.1038/86684.
- Welsh DK, Noguchi T. 2012. Cellular bioluminescence imaging. *Cold Spring Harbor protocols*, 2012 (8). DOI 10.1101/pdb.top070607.
- Wu M, Shu J. 2018. Multimodal Molecular Imaging: Current Status and Future Directions. *Contrast media & molecular imaging*, 2018: 1382183. DOI 10.1155/2018/1382183.
- Xu H, Rice BW. 2009. In-vivo fluorescence imaging with a multivariate curve resolution spectral unmixing technique. *Journal of biomedical optics*, 14 (6): 64011. DOI 10.1117/1.3258838.
- Youn H, Hong K-J. 2012. In vivo Noninvasive Small Animal Molecular Imaging. *Osong public health and research perspectives*, 3 (1): 48–59. DOI 10.1016/j.phrp.2012.02.002.
- Zakeri A, Kouhbanani MAJ, Beheshtkhoo N, Beigi V, Mousavi SM, Hashemi SAR, Karimi Zade A, Amani AM, Savardashtaki A, Mirzaei E, Jahandideh S, Movahedpour A. 2018. Polyethylenimine-based nanocarriers in co-delivery of drug and gene: a developing horizon. *Nano reviews & experiments*, 9 (1): 1488497. DOI 10.1080/20022727.2018.1488497.
- Zhao M-X, Zhu B-J. 2016. The Research and Applications of Quantum Dots as Nano-Carriers for Targeted Drug Delivery and Cancer Therapy. *Nanoscale research letters*, 11 (1): 207. DOI 10.1186/s11671-016-1394-9.
- Zhou Z, Qu J, He L, Peng H, Chen P, Zhou Y. 2018.  $\alpha 6$ -Integrin alternative splicing: distinct cytoplasmic variants in stem cell fate specification and niche interaction. *Stem cell research & therapy*, 9 (1): 122. DOI 10.1186/s13287-018-0868-3.
- Zinn KR, Chaudhuri TR, Szafran AA, O'Quinn D, Weaver C, Dugger K, Lamar D, Kesterson RA, Wang X, Frank SJ. 2009. Noninvasive Bioluminescence Imaging in Small Animals, 26.
- Zintchenko A, Susha AS, Concia M, Feldmann J, Wagner E, Rogach AL, Ogris M. 2009. Drug nanocarriers labeled with near-infrared-emitting quantum dots (quantoplexes): imaging fast dynamics of distribution in living animals. *Molecular therapy : the journal of the American Society of Gene Therapy*, 17 (11): 1849–1856. DOI 10.1038/mt.2009.201.

Figure 1: Comparison of T1 and T2 weighted MR imaging mechanism.....	6
Figure 2: Overview of the IVIS Spectrum CT.....	9
Figure 3: Schematic comparison of Epi- (A) and Transillumination (B).....	11
Figure 4: Fluorescent emission spectra of food, NIR window.....	12
Figure 5: Absorption coefficients of Hb, HbO <sub>2</sub> and H <sub>2</sub> O.....	13
Figure 6: Emission spectra of QDs.....	14
Figure 7: Luciferin-luciferase reaction.....	16
Figure 8: Schematic PEG- Nanoparticle.....	19
Figure 9: Schematic opsonization of CD47- SIRP $\alpha$ interaction by antibodies.....	22
Figure 10: Schematic intratracheal instillation.....	25
Figure 11: Timeline of the QD project.....	29
Figure 12: Timeline of the Auropolyplex project.....	30
Figure 13: Timeline of the CD49f project.....	31
Figure 14: Timeline of the CD47 project.....	32
Figure 15: 0h epifluorescence imaging after QD application.....	39
Figure 16: 24h epifluorescence imaging after QD application.....	40
Figure 17: 24h epifluorescence imaging of organs ex vivo after QD application.....	41
Figure 18: 0h epifluorescence imaging of auropolyplexes.....	42
Figure 19: 24h epifluorescence imaging of auropolyplexes.....	43
Figure 20: FLI biodistribution of AF750-siRNA after i.t. application in prone position.....	44
Figure 21: FLI biodistribution of AF750-siRNA after i.t. application in supine position.....	44
Figure 22: FLIT/CT imaging of AF750-siRNA after i.t. application.....	45
Figure 23: 24h FLI of organs ex vivo after i.t. AF750 siRNA AuNP application.....	46
Figure 24: BLI after injection of LPEI-PEG and LPEI- PEG- CD49f.....	48
Figure 25: BLI signal intensity comparison of LPEI- PEG and LPEI-PEG-CD49f animals.....	49
Figure 26: BLI 8 days after injection of MDA-MB-231 EGFP <sub>luc</sub> cells.....	51
Figure 27: Timescale of BLI signal strength after injection MDA-MB-231 EGFP <sub>luc</sub> cells.....	52
Figure 28: Supplementary FLIT QDs data.....	56
Figure 29: Supplementary FLIT QDs data.....	57
Figure 30: Supplementary FLI auropolyplex data.....	58
Figure 31: Supplementary FLI auropolyplex data.....	59
Figure 32: Supplementary auropolyplex FLIT/CT data.....	60
Figure 33: Supplementary BLI CD49f data.....	61
Figure 34: Supplementary BLI CD49f data.....	62

Figure 35: Supplementary BLI CD47 data.....	63
---	----